AFRL-AFOSR-UK-TR-2020-0025

Passive Hypersonic Transition Control by Means of Ultrasonically Absorptive Thermal Protection Materials (UAT)

Alexander Wagner
DEUTSCHES ZENTRUM FUR LUFT- UND RAUMFAHRT E.V.
LINDER HOHE, KA
KOLN, 51147
DE

06/10/2020
Final Report

Air Force Research Laboratory
Air Force Office of Scientific Research
European Office of Aerospace Research and Development
Unit 4515 Box 14, APO AE 09421

REPORT DOCUMENTATION PAGE

Form Approved
OMB No. 0704-0188

1. REPORT DATE *(DD-MM-YYYY)*	2. REPORT TYPE	3. DATES COVERED *(From - To)*
10-06-2020	Final	30 Sep 2016 to 29 Sep 2019

4. TITLE AND SUBTITLE
Passive Hypersonic Transition Control by Means of Ultrasonically Absorptive Thermal Protection Materials (UAT)

5a. CONTRACT NUMBER

5b. GRANT NUMBER
FA9550-16-1-0456

5c. PROGRAM ELEMENT NUMBER
61102F

6. AUTHOR(S)
Alexander Wagner

5d. PROJECT NUMBER

5e. TASK NUMBER

5f. WORK UNIT NUMBER

7. PERFORMING ORGANIZATION NAME(S) AND ADDRESS(ES)
DEUTSCHES ZENTRUM FUR LUFT- UND RAUMFAHRT E.V.
LINDER HOHE, KA
KOLN, 51147 DE

8. PERFORMING ORGANIZATION REPORT NUMBER

9. SPONSORING/MONITORING AGENCY NAME(S) AND ADDRESS(ES)
EOARD
Unit 4515
APO AE 09421-4515

10. SPONSOR/MONITOR'S ACRONYM(S)
AFRL/AFOSR IOE

11. SPONSOR/MONITOR'S REPORT NUMBER(S)
AFRL-AFOSR-UK-TR-2020-0025

12. DISTRIBUTION/AVAILABILITY STATEMENT
A DISTRIBUTION UNLIMITED: PB Public Release

13. SUPPLEMENTARY NOTES

14. ABSTRACT
A temperature stable porous C/C-SiC based material was successfully developed, acoustically characterized, experimentally tested and numerically modeled. The new generation ultrasonically absorptive material extents the applicability of the material towards an Ultrasonically Absorptive Thermal Protection System (UAT). In summary, the results have shown that the properties of the material can be adapted both by changing the CFRP production process and by changing the resin system. The new UAT material was successfully integrated and instrumented into a 7 degree half angle cone for testing in the DLR High Enthalpy Shock Tunnel Goettingen (HEG) at Mach 7.4. The tests ultimately confirmed the strongly increased absorber performance compared to the original C/C. Second mode instabilities were found to be strongly damped, making the detection of the waves above the porous surface very challenging. The increased absorber performance led to a strong delay of boundary layer transition which was the main purpose of the project.

15. SUBJECT TERMS
hypersonic flow, passive transition control, thermal protection, ultrasonically absorptive

16. SECURITY CLASSIFICATION OF:			17. LIMITATION OF ABSTRACT	18. NUMBER OF PAGES	19a. NAME OF RESPONSIBLE PERSON
a. REPORT	b. ABSTRACT	c. THIS PAGE			SMITH, DOUGLAS
Unclassified	Unclassified	Unclassified	SAR		19b. TELEPHONE NUMBER *(Include area code)* 314-235-6013

Standard Form 298 (Rev. 8/98)
Prescribed by ANSI Std. Z39.18

DLR IB-XXX

Passive Hypersonic Transition Control by Means of Ultrasonically Absorptive Thermal Protection Materials (UAT)

FINAL REPORT

DLR

Document properties

Title	Passive Hypersonic Transition Control by Means of **U**ltrasonically **A**bsorptive **T**hermal Protection Materials (UAT)
Subject	FINAL REPORT
Project Type	Grant/Cooperative Agreement Award
PI	Dr. Alexander Wagner (DLR-GO)
Coauthors	Dr. Viola Wartemann (DLR-BS), Christian Dittert (DLR-ST), Marius Kütemeyer (DLR-ST)
Grant Number	FA9550-16-1-0456
Period	29.09.2016 to 28.09.2019
Date	9th of December 2019
Version	1.0
File Path	FinalReport

Contents

1. Summary

A temperature stable porous C/C-SiC based material was successfully developed, acoustically characterized, experimentally tested and numerically modeled. The new generation ultrasonically absorptive material extents the applicability of the material towards an Ultrasonically Absorptive Thermal Protection System (UAT).
The conclusions in each development field are summarized below.

1.1. Materials

In summary, the results have shown that the properties of the material can be adapted both by changing the CFRP production process and by changing the resin system. However, this change is particularly noticeable in the C/C intermediate state of the materials. In the final C/C-SiC, these changes are partially reversed by siliconization. The most significant difference to the classic C/C can be seen in the pore distribution as well as in the length specific flow resistance, which is much lower for the the C/C-SiC materials and beneficial if an application as ultrasonic absorber is envisaged. The porosity of the porous C/C-SiC is in the same order of magnitude as for the classic C/C with the exception of the HP-1 plate. Overall, the AK-1 and RTM-1 materials have to be highlighted in terms of their properties. Both materials are easy to reproduce and show the typical fiber-reinforced block structure in C/C-SiC. Compared to them, HP-1 and RTM-2 are showing a very high porosity, especially in C/C, but they are significantly lower in strength and failure tolerance due to their partly monolithic characteristics.
For the subsequent HEG tests the AK-1 material was considered as the material, which is faster, cheaper and more reproducible to produce than the other materials and at the same time offer a significantly increased acoustic absorber characteristic compared to the initial (classic) C/C.
In addition, surface analyses have shown that the pores- and porosity- distribution within the first millimeter can deviate significantly from to the volumetric properties due to mechanical processing. The latter effect is respected in the flow through resistance measurements and the direct reflection coefficient measurements which are, besides porosity, the main parameter used to characterize the acoustic performance of the material. The bench test used for reflection coefficient measurements could be optimized to reach flight relevant static pressures and frequencies, the latter up to 490 kHz. Particular focus was set on determining the measurement uncertainties allowing to differentiate between measurement errors and locally changing surface properties.

1.2. Experimental Testing

The new UAT material was successfully integrated and instrumented into a 7 degree half angle cone for testing in the DLR High Enthalpy Shock Tunnel Göttingen (HEG) at Mach 7.4. The tests ultimately confirmed the strongly increased absorber performance compared to the original C/C. Second mode instabilities were found to be strongly damped, making the detection of the waves

above the porous surface very challenging. The increased absorber performance led to a strong delay of boundary layer transition which was the main purpose of the project.

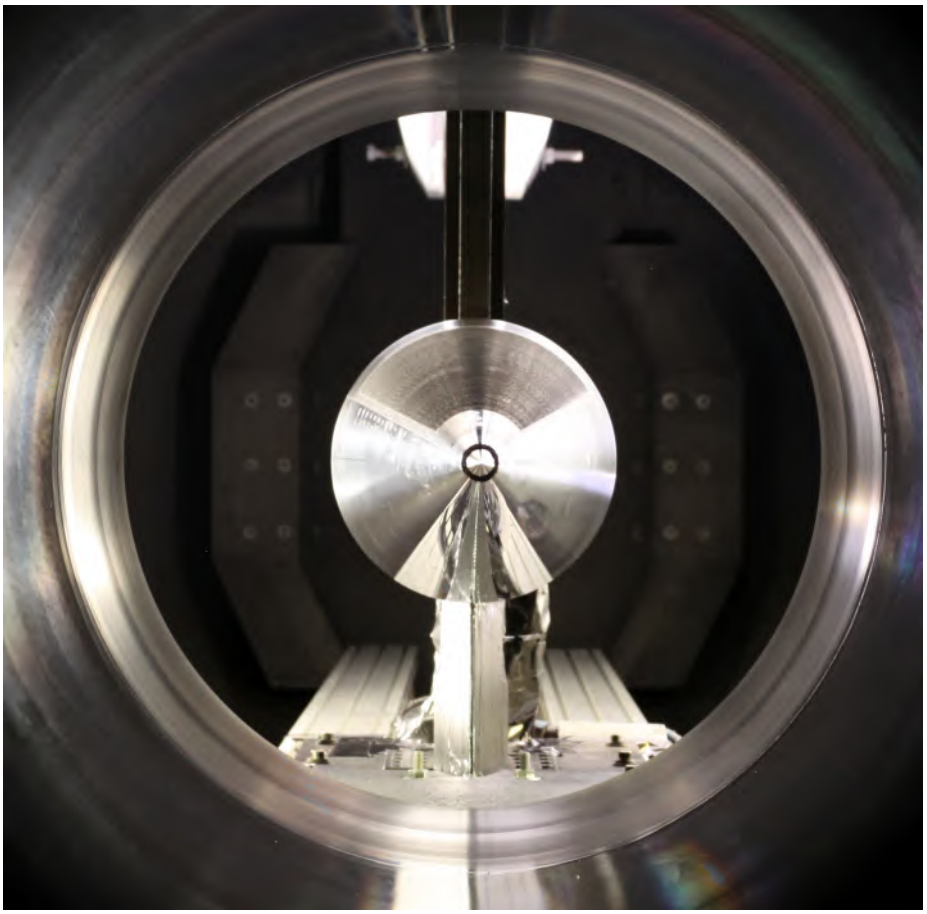

1-1 Cone model with the CC-SiC insert on the top in the HEG test section. Picture taken through the nozzle throat.

1.3. Numerical Rebuild

The numerical predictions for C/C-SiC delivers a lower damping of the second modes and consequently a lower transition shift as visible in the experiments in HEG. A possible reason could be a deviation in the assumed material properties (see table 6-2). Recent findings towards the end of the project revealded a change of the functions of the structure factor and the flow resistivity of table 6-2 by considering rarefied gas effects. Another explanation is the higher surface porosity illustrated in figure 4-13, which could no be respected in the LST analysis since the LST calculations assumed a porosity, based on the overall volume porosity, which might by lower than the surface porosity after amchining the material. A complete reproduction of the varying porosity along the depth is only possible with DNS. Nevertheless, the numerical investigations demonstrate, as in the experiments, an improvement of the absorber performance (comparing C/C with C/C-SiC) with respect to the second mode damping and the resulting transition delay.

2. Introduction

The present study combines an experimental and numerical investigation aiming to develop a material which is ultrasonically absorptive and at the same time high temperature resistant. We use the abbreviation **UAT - Ultrasonically Absorptive Thermal Protection** for that class of material to allow a differentiation towards the well known **UAC** material (ultrasonically absorptive coating).

Laminar to turbulent transition in high-speed boundary layers leads to a significant increase of shear stress and heat flux. Thus, the performance and the thermal protection system of hypersonic vehicles and re-entry vehicles are strongly affected. Particularly with regard to hypersonic sustained flight, the increase of the laminar portion of the boundary layer is of critical importance. Previous studies proved that hypersonic boundary layers, in which the second-mode instability dominates the transition process, can be stabilized by means of ultrasonically absorptive coatings. The concept was confirmed theoretically by Fedorov et al. (2001) and experimentally by Rasheed et al. (2002) and Fedorov et al. (2006) using ultrasonically absorptive materials with regular microstructures. Based on the promising results obtained on porous surfaces and the fact that the majority of the thermal protection materials exhibit a natural porosity, Wagner et al. (2013a, 2014) and Wartemann et al. (2014) for the first time investigated ultrasonically absorptive fiber reinforced ceramics with the potential for use as thermal protection materials. The studied carbon fiber reinforced carbon ceramic offered moderate temperature stability only which does not allow an application as TPS in a wide range. However, the used material is an intermediate state of the C/C-SiC which in contrast is oxidation resistant up to 2000K and was used successfully as TPS on reentry vehicles, (Weihs et al., 2001; Reimer, 2006; Weihs, 2013a), and hypersonic vehicles, (Glass et al., 2014).

The conducted study succesfully aimed to develop a high temperature resistant fiber reinforced materials based on C/C-SiC with appropriate ultrasonic absorption properties. The material combines TPS and passive hypersonic transition control capabilities and could be highly beneficial for the development of future aircraft operating in the regime of hypersonic sustained flight.

2.1. Test Conditions of Interest with Respect to the HEG Test Envelope

The present section reviews possible application ranges for hypersonic transition control by means of porous coatings. Due to the lack of information on flight vehicles and corresponding trajectory the review concentrates on generic geometries as investigated in the scope of the HIFiRE flight test program. The purpose of the section is to identify flight conditions which overlap with the HEG test envelope to prepare for the next step after a successful ground test of the UAT materials.

Please note, that an analysis of any predominantly 2-D geometry at any given point of operation would be feasible as well if interest is expressed.

2.1.1. Flight Testing

In general, controlling boundary layer transition with porous surfaces is applicable on slender vehicles flying at sufficiently high Mach number and small angle of attack. A predominantly 2D boundary layer and a boundary layer edge Mach numbers above 4 in combination with cooled vehicle walls (as it typically is the case for during hypersonic flight) allow the second mode wave to develop as the dominant boundary layer instability. This in return provides the opportunity to manipulate the acoustic wave type disturbance using an acoustically absorptive surface and leading to a passive boundary layer transition control.

2.1.1.1. HIFiRE I

The HIFiRE I flight experiment is a well documented flight test with a blunted 7 degree half angle cone - cylinder - flare configuration. Figure 2-1 provides a schematic view of the configuration together with an altitude distribution over time. The latter indicates the test phase during the ascent and descent phase of the flight model.

Figure 2-2 provides the unit Reynolds number versus Mach number distribution during ascent and descent. It can be seen that near the end of the descent phase unit Reynolds numbers and Mach numbers are reached which allow a transitional boundary layer with second mode presence based on experience gathered in HEG at similar test conditions and identical model geometry. The red rectangular in figure 2-2 marks the Reynolds-Mach range in which HEG is operated to investigate this type of flow fields.

In conclusion, the HIFiRE I flight trajectory provides an excellent test case for comparative studies in HEG and during in flight with respect to the application of UAT for passive transition control.

Currently, the UAT project group is in contact with the US Air Force Research Laboratory discussing a potential flight test on the HIFLIER I flight experiment which is expected to have a similar trajectory compared to HIFiRE I.

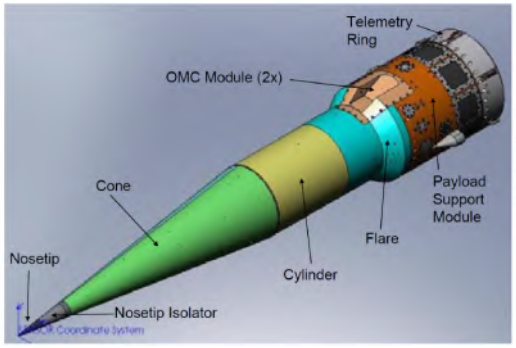

(a) Schematic view

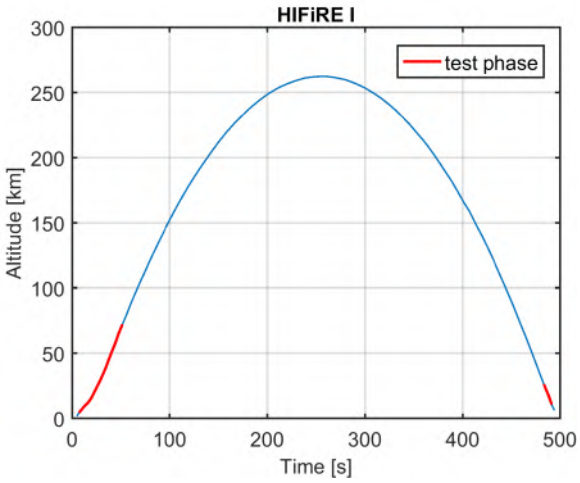

(b) Altitude over time

2-1 HIFiRE 1: flight trajectory

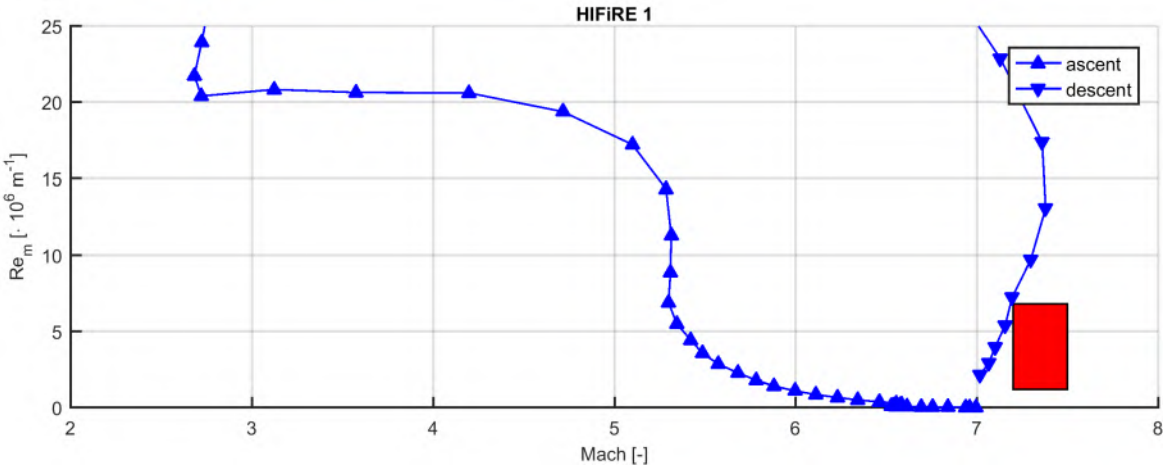

2-2 HIFiRE 1: Unit Reynolds number versus free-stream Mach number. The red marker identifies the approximate HEG test range at Mach 7.4 .

2.1.1.2. HIFiRE 5 - C

The HIFiRE 5C flight test has a very similar trajectory compared to HIFiRE I, shown figure 2-3 providing altitude versus time. As figure 2-4 indicates, the the Mach number and unit Reynolds number during descent match the HEG test range at Mach 7 even better. However, HIFiRE 5C is designed as an elliptic cone flying at angle of attack. This introduces 3D effects into the boundary layer such as cross flow instabilities. The latter quickly become the dominant transition mechanism. Thus, UAT would only be of use at small angle of attack as long as second mode dominated transition plays a significant role.

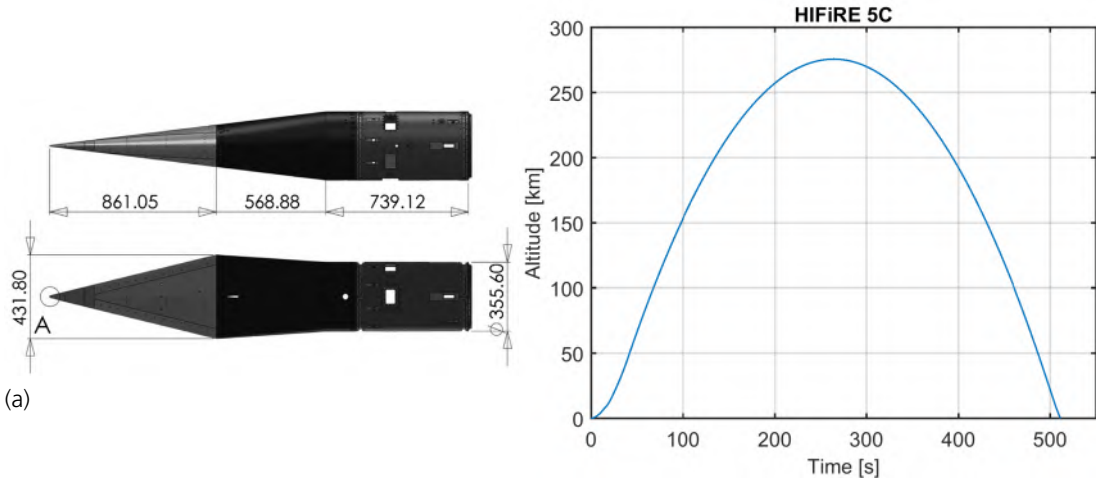

2-3 HIFiRE 5C flight trajectory

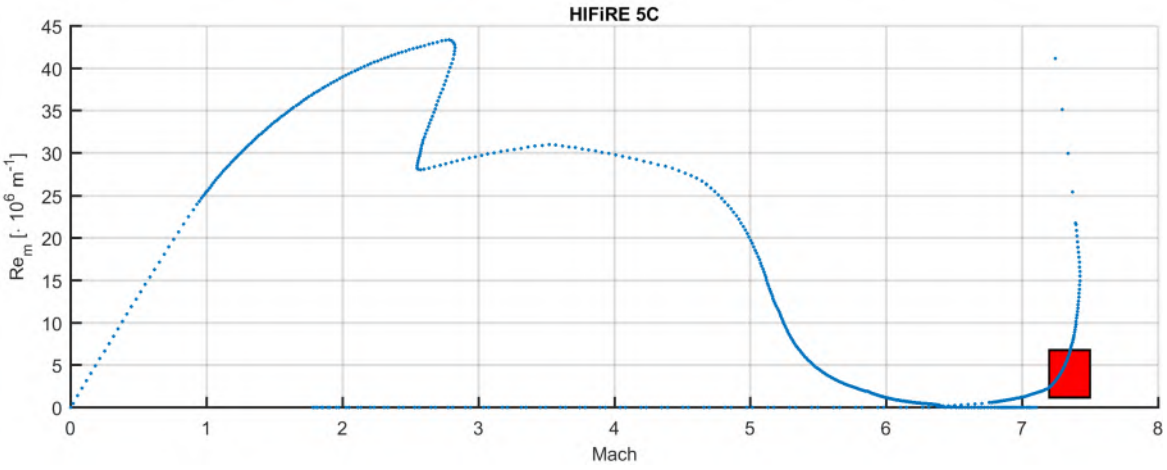

2-4 HIFiRE 5C: Unit Reynolds number versus free-stream Mach number. The red marker identifies the approximate HEG test range at Mach 7.4 .

2.1.1.3. HIFiRE 8

HIFiRE 8 focuses on the operation of a scramjet at about Mach 8. As depicted in figure 2-5 and 2-6 the targeted test conditions are reached at the end of the ascent phase at about 30 km altitude. The Mach number and Reynolds number range at those test conditions seem to be very promising with respect to the use of UAT. Relevant vehicle sections to be realized in UAT materials could be for instance the upper vehicle surface starting at the nose as well as the ramp like surface just upstream the intake.

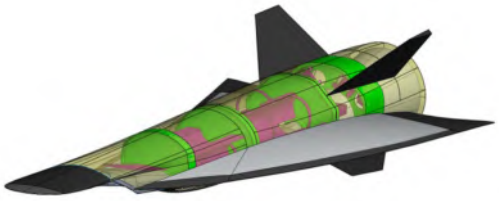

(a)

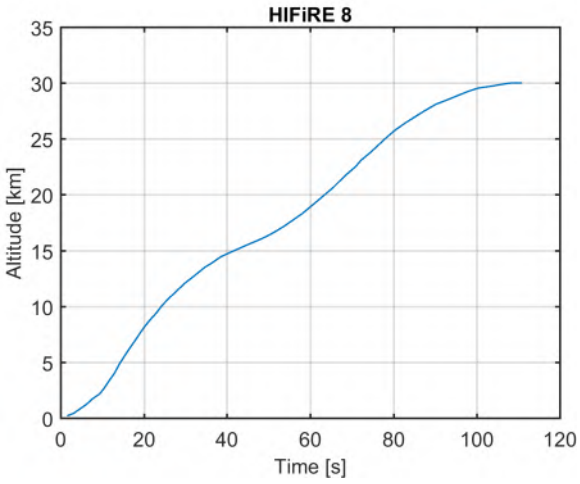

(b)

2-5 HIFiRE 8 flight trajectory

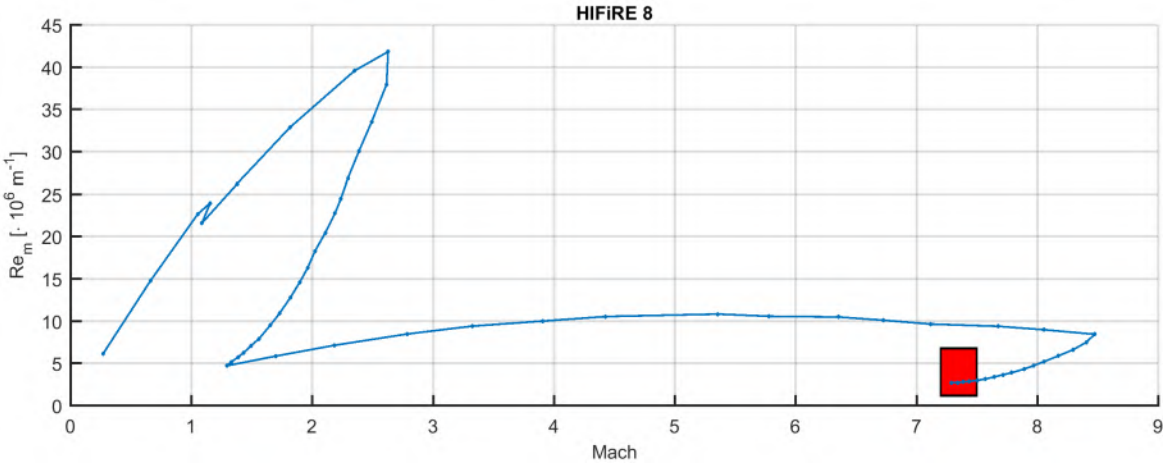

2-6 HIFiRE 8: Unit Reynolds number versus free-stream Mach number. The red marker identifies the approximate HEG test range at Mach 7.4 .

2.2. Relevant HEG Test Conditions

To support of the study table 2-1 provides an overview on the HEG test conditions relevant for the present study.

$Re_m[m^{-1}]$	$1.46 \cdot 10^6$	$2.4 \cdot 10^6$	$4.0 \cdot 10^6$	$6.4 \cdot 10^6$	$1.5 \cdot 10^6$, high h_0
p_0 $[MPa]$	6.8 (4.2%)	12.7 (1.7%)	19.2 (4.2%)	28.4 (3.6%)	40.0 (1.5%)
T_0 $[K]$	2720 (2.2%)	2895 (1.6%)	2734 (1.1%)	2582 (1.0%)	6800 (1.0%)
h_0 $[MJ/kg]$	3.25 (6.0%)	3.48 (2.0%)	3.24 (1.4%)	3.03 (0.9%)	11.9 (1.4%)
M_∞ $[-]$	7.3 (0.2%)	7.3(0.2%)	7.4 (0.2%)	7.4 (0.2%)	6.1 (0.1%)
p_∞ $[Pa]$	789 (3.4%)	1453 (2.2%)	2129 (4.0%)	3083 (3.9%)	6820 (1.37%)
T_∞ $[K]$	267 (1.7%)	285 (2.3%)	268 (2.1%)	248 (1.5%)	1320 (0.5%)
ρ_∞ $[g/m^3]$	10.2 (2.5%)	17.7 (2.2%)	27.6 (4.8%)	43.2 (2.8%)	17.3 (1.9%)
u_∞ $[m/s]$	2409 (0.7%)	2480 (0.9%)	2422 (0.8%)	2350 (0.6%)	4406 (0.3%)
Re_m $[10^6 m^{-1}]$	1.46 (2.7%)	2.43 (2.9%)	4.06 (4.2%)	6.39 (2.3%)	1.5 (2.7%)

2-1 Averaged HEG test conditions and standard deviations.

Furthermore, the heat flux distributions along a 7 degree half angle cone, previously tested in HEG, is provided in figure 2-7 for various nose radii and unit Reynolds numbers. The latter plot quickly provides information on the approximate transition location on the cone an thus suitable approximate locations for a porous insert for passive transition delay.

In addition to the transition locations, the observed second mode frequencies are of interest for the absorber design. Therefore, figure 2-8 provides an overview on the measured instability frequencies on cones in HEG. The data is obtained using PCB and ALTP transducers. Additional information could be extracted from high speed schlieren visualizations.

The provided overview on a large number of tests conducted in HEG supported the layout of the experiments planned to be conducted in the scope of the present study.

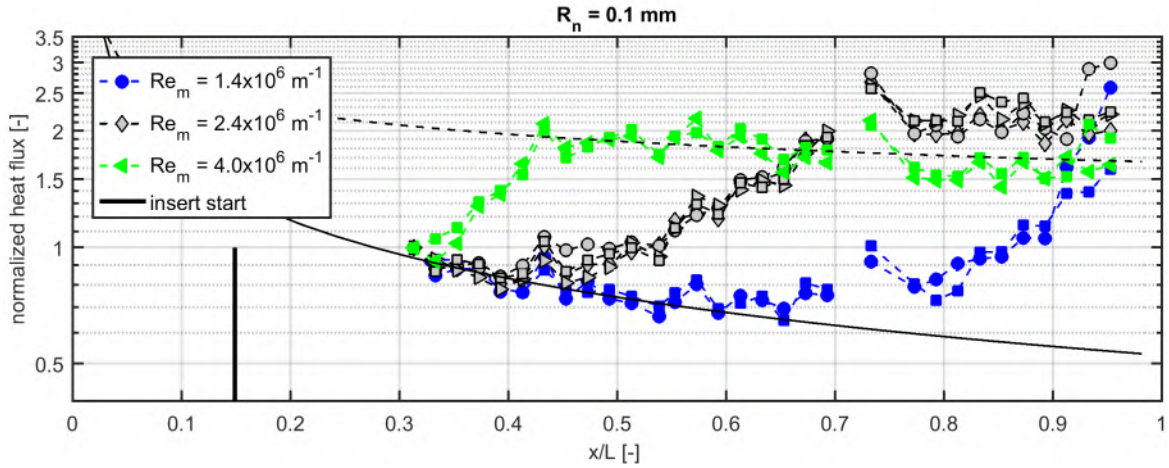

(a)

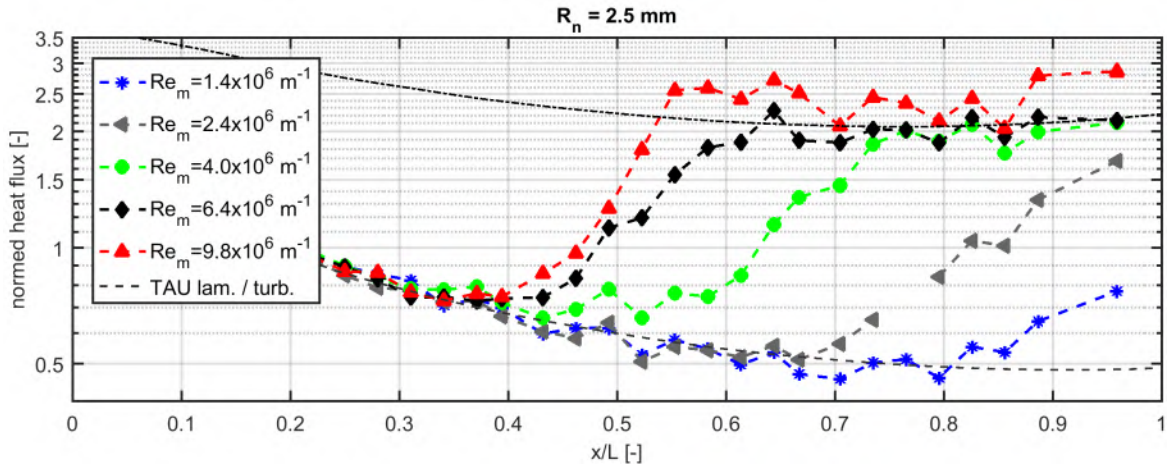

(b)

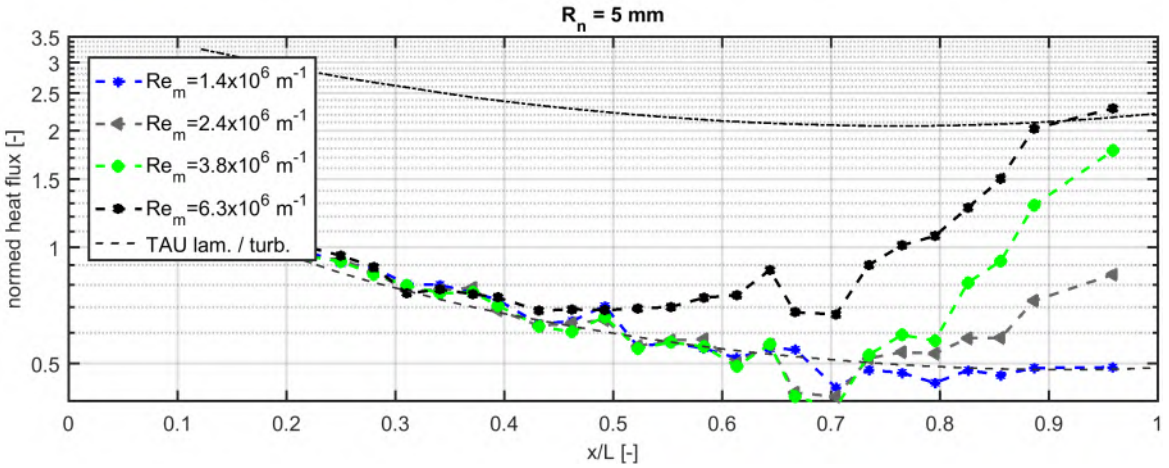

(c)

2-7 Heat flux distribution along the 7 degree half angle cone for different nose radii and unit Reynolds numbers.

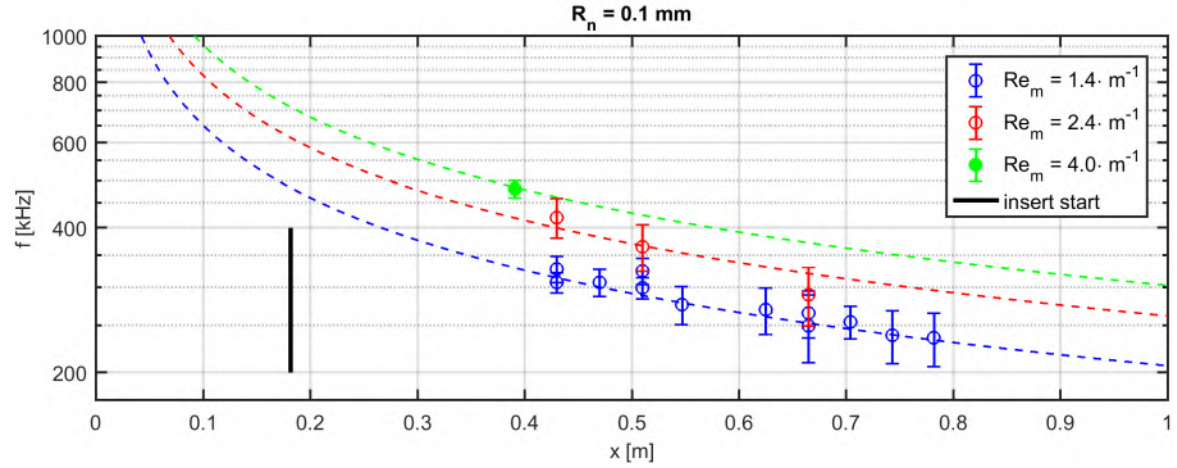

(a)

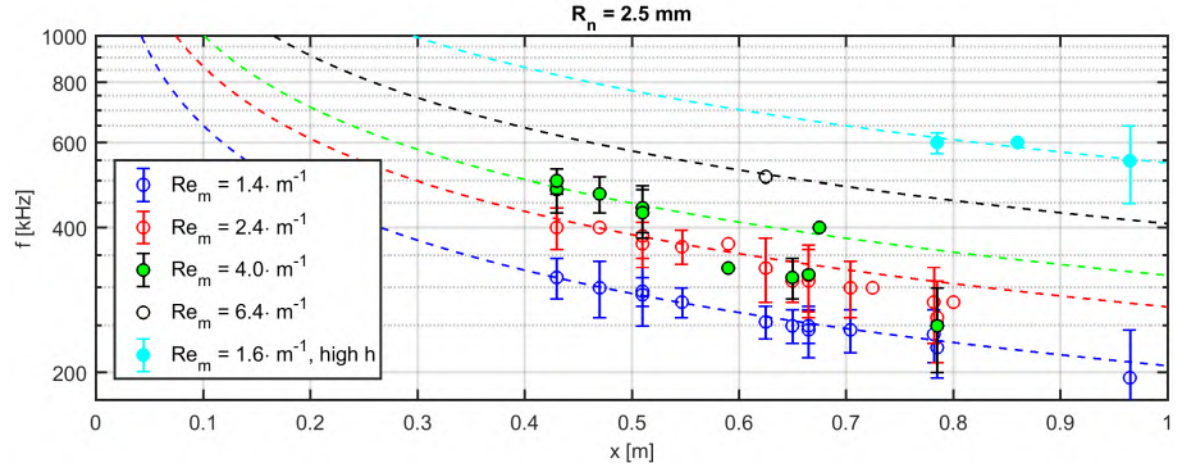

(b)

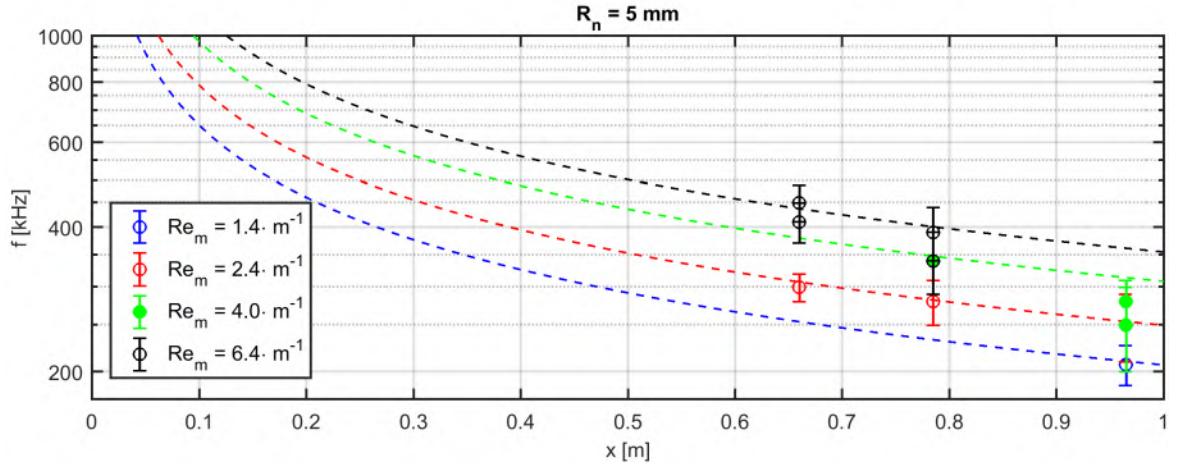

(c)

2-8 Second mode frequency distribution along the 7 degree half angle cone for different nose radii and unit Reynolds numbers.

3. Material Development

3.1. Manufactering Processes

There are different industrial processes to manufacture CMC materials. Chemical Vapor Infiltration (CVI), Polymer Infiltration and Pyrolysis (PIP), Liquid Polymer Infiltration (LPI), hot isostatic pressing (HIP) and Liquid Silicon Infiltration (LSI) are used in general for this purpose. The CVI process usually achieves the highest mechanical strength and elongation, however this procedure is very time-consuming and expensive. An overview of the manufacturing processes can be found in Krenkel (2008).

At DLR Stuttgart, the CMC manufacturing is based on the liquid silicon infiltration (LSI) process. Carbon fiber reinforced silicon carbide (C/C-SiC) is especially suitable for use as thermal protection system as shown by Zuber et al. (2010); Weihs (2013b). In addition to the comparatively low-cost production of the CMC material by LSI, the process has the advantage that the material can be optimized between the several stages of the process.

The LSI process can be divided up into three main steps. In a first step, a green body of carbon fiber reinforced plastic (CFRP) is formed via autoclave, resin transfer moulding (RTM) or hot pressing techniques using commercially available $0°/90°$ carbon fabrics impregnated with a phenolic resin. After curing, the green body is pyrolyzed in a second step at temperatures of up to $1650°C$, which converts the phenolic matrix to amorphous carbon. Due to the volume shrinkage of the matrix and the geometrical stability of the C fiber architecture, internal stresses are built up, leading to microcracks and a porous C/C preform. In order to obtain C/C-SiC, the C/C material has to be siliconized by means of liquid silicon infiltration by capillary forces at $T > 1420°C$ (Krenkel, 2008). An overview of the main steps is shown in figure 3-1.

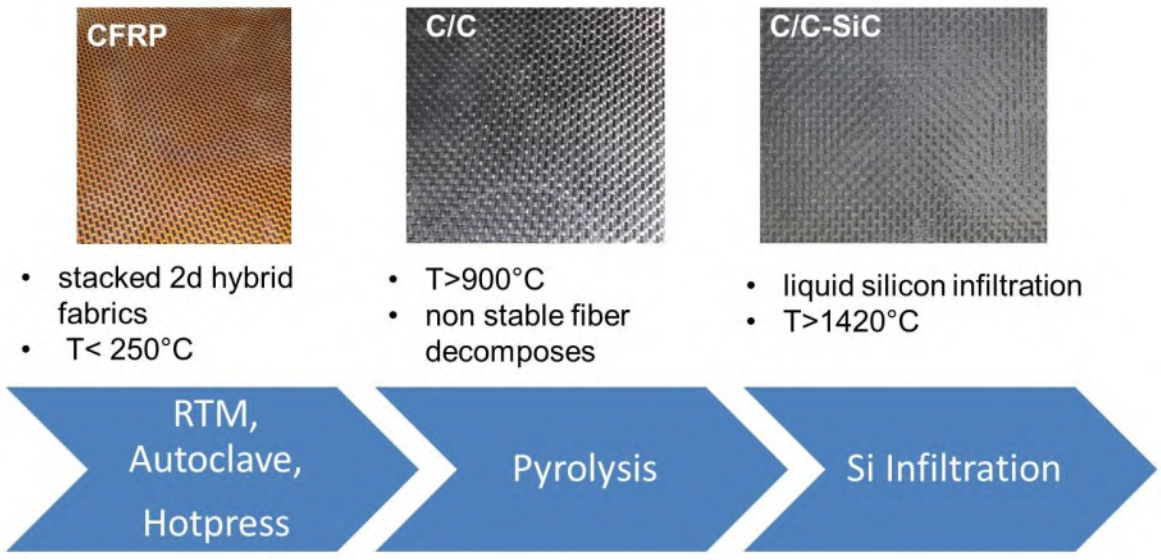

3-1 Overview main LSI manufacturing steps.

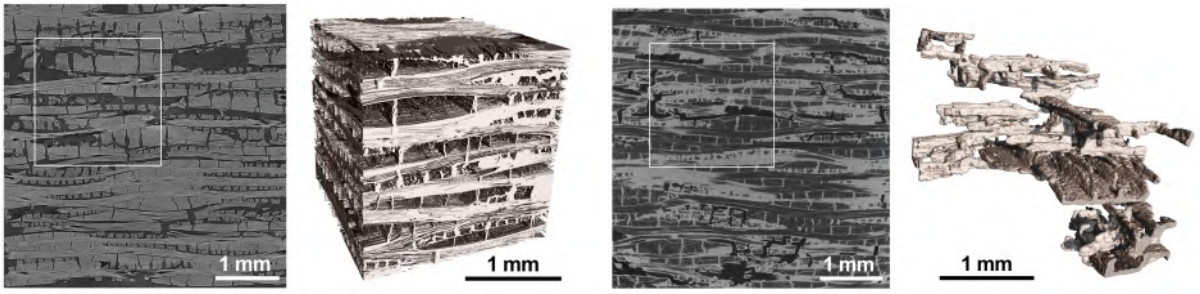

3-2 X-ray CT image of the pore structure of porous C/C (left) and C/C-SiC (right) manufactured from hybrid fabrics. Dittert and Kütemeyer (2017)

As mentioned, C/C is an intermediate product of this material process after pyrolysis. It is very favorable as it offers an open-porous micro structure, which is suitable as ultrasonically absorbing TPS material (Wagner, 2014a). However, compared to C/C-SiC, C/C exhibits some disadvantages; especially the oxidation resistance of C/C compared to SiC-based materials and its decreased mechanical strength is considered critical.
To close the gap between C/C and C/C-SiC, a new material development based on C/C-SiC fiber reinforced ceramics started at DLR Stuttgart. Contrary to the dense C/C-SiC materials, it has a porosity and permeability like C/C, which can be additionally adapted to the application purpose. Compared to C/C however, the oxidation resistance is significantly improved. The optimization of the material is done through a selective insertion of cavities into the C/C by replacing carbon fibers by non-stable fiber material before pyrolysis. During pyrolysis, these fibers will be degraded, forming a higher porosity (Dittert and Kütemeyer, 2017). Contrary to the dense C/C-SiC material, the CFRP green body for a high porous C/C-SiC was made from 2D hybrid fabrics with a roving size of 3K. Furthermore, the hybrid fabric used was a mix of carbon and aramid fibers with a composition of 38.80% aramid fibers and 61.20% carbon fibers. In Figure 3-2, the optimized material is shown after pyrolysis at its C/C state and after final siliconization.
The focus during this project is to further develop the introduced porous C/C-SiC material shown in figure 3-2 and to optimize this material with regards to its UAT capabilities.

3.2. CFRP Variations

The influence of CFRP production process on the porosity and channel structure of C/C-SiC material is investigated during this project. The intention is to evaluate the resulting CMC materials on the basis of their acoustic properties, especially porosity, length specific flow resistance, pore distribution and mechanical properties and thus to identify the most effective CFRP process. As mentioned before there are basically three processes available for CFRP production.

Hot pressing is a process in which plastics are processed in metal molds under pressure and at temperatures above $120°C$. The process is particularly suitable for the processing of short-fiber rein-

forced plastics. Short fibers, resin precursors and additives are mixed and pressed into shape. When processing long fibers, the process is used as a variation of wet pressing. The fibers are inserted into the die and impregnated with resin before the press tool is closed. The dry fabric is infiltrated with resin through a hose during the pressing cycle. The mold is heated by the two heating/cooling plates and the pressing chamber can be evacuated. It is evacuated to minimize air entrapment in the fabric layers as well as to remove evaporating gases and water vapor from the resin. The contact pressure is set via the traverse path of the press. Compared to resin injection and autoclave processes, no additional atmospheric pressure is applied during heating.

For the **autoclave process**, pre-impregnated semi-finished fiber products are used. The prepregs are laminated into a one-piece mold, vacuum-packed and cured in a heatable pressure vessel. Pressures up to 10 bar and temperatures of $200°C$ are common (Krenkel, 2008).

Resin Transfer Molding (RTM) is a resin injection process in which the fabric is inserted into a mold, the resin is being placed in an extra chamber. By building up a pressure difference between the fiber and resin chamber, the fabric is gradually infiltrated with resin. By heating the mold, infiltration and curing can be combined. The advantage here is that the closed system also allows thick-walled, three-dimensional components to be produced close to the final contour.

All CFRP green bodies were made from commercial available 2D hybrid fabrics with a roving size of 3K. Furthermore, the hybrid fabric used, was a mix of carbon and aramid fibers with a composition of 38.80% aramid fibers and 61.20% carbon fibers. The textile wave pattern was 3/1 twill and is shown with the hybrid fabric in figure 3-3. The cutting of the fabric was done by a CAD based digital cutting system manufactured by Zünd. Since for the autoclave process prepregs are used, the hybrid fabric was industrially preimpregnated. For the other two CFRP processes a suitable phenolic

3-3 Hybrid fabric, 3/1 twill.

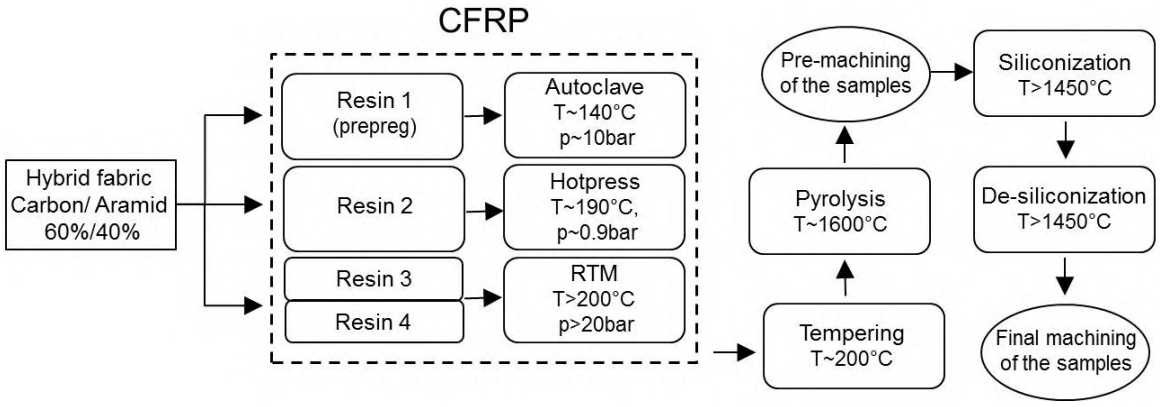

3-4 Scheme of the CMC manufacturing process.

resin was chosen. In addition, the influence of a second resin system compared to standard phenolic resin was investigated for the RTM process.
In figure 3-4 an overview of the complete C/C-SiC manufacturing process is shown.

As already mentioned and shown in Fig. 3-4, the process steps after the CFRP production are identical for all materials. During tempering the internal stresses are reduced. Tempering takes place above the curing temperature of the resin and over a period of 24 h. Pyrolysis is carried out over a period of several days at a maximum temperature of $1650°C$. Several temperature levels are used, as the highest mass loss of aramid fibers for example, takes place at $500-600°C$. Siliconization takes place in fine vacuum at a maximum temperature from $1650°C$. The samples are siliconized with an excess supply of silicon granules. Finally, the free silicon is thermally removed from the samples during de-siliconization. The final C/C-SiC plates manufactured during this process can now be evaluated with regards to their acoustic properties.

3.3. Obtained Samples

Table 3-1 shows an overview of the green bodies, manufactured with help of the presented CFRP processes. An exception to this is the so-called "classic C/C", which has already been extensively characterized and for which an application as an absorber material has been shown by (Wagner,

Name	CFRP-process	comments
AK-1	autoclave	prepreg
HP-1	hotpress	phenolic resin
RTM-1	RTM	phenolic resin
RTM-2	RTM	microporous resin
classic C/C	autoclave	characterized in (Wagner, 2014a)

3-1 Produced plates, names and the process used for manufacturing.

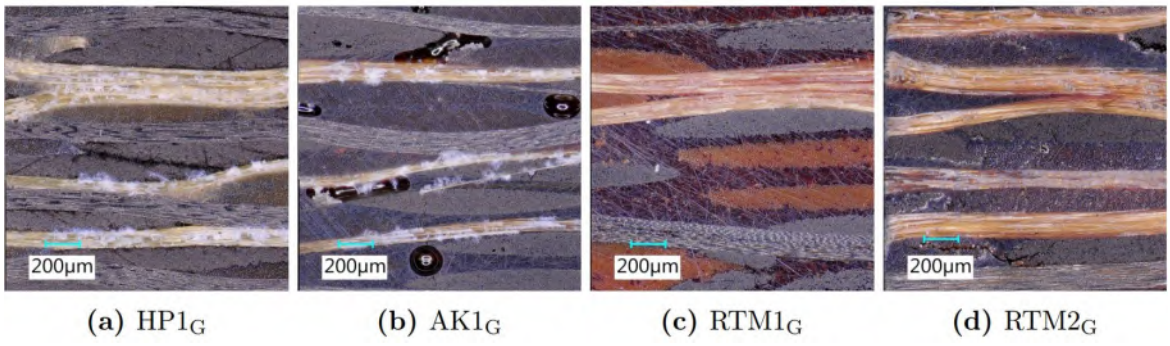

3-5 Reflected light microscope images of the CFRP bodies. The cut is perpendicular to the fabric plane. Dömling (2018)

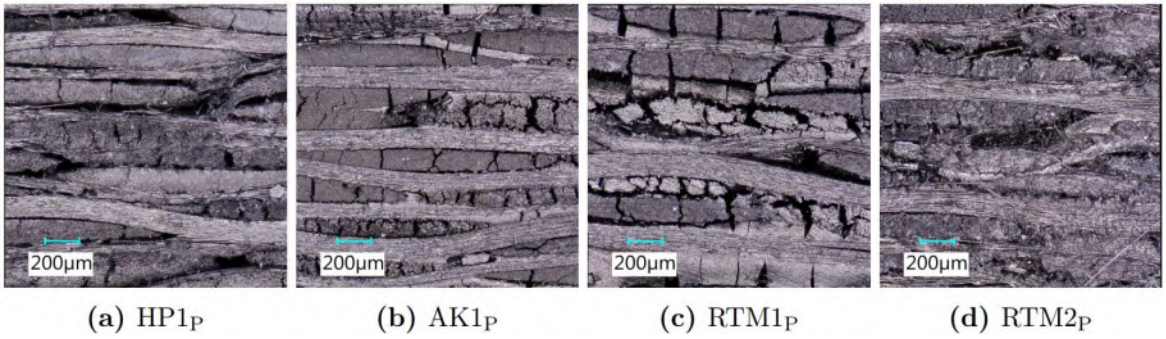

3-6 Reflected light microscope images of the C/C bodies after pyrolysis. The cut is perpendicular to the fabric plane. Dömling (2018)

2014a; Wagner et al., 2015). This material is made only from standard carbon fibers and is shown here for comparison purposes.

The quality of the green body is essential for the properties of the final CMC made from it. Classic manufacturing defects in the CFRP are variations in fiber arrangement, inhomogeneous resin distribution, pores, microcracks, debonding and delaminations.Dömling (2018) was investigating the samples in their CFRP an C/C state by taking microscopic images. In Figure 3-5 microscope images of the samples in their CFRP state are shown. The plate HP1 manufactured with the hotpress technique shows gaps within the structure. Cracks and debonding are also visible. The crack structure is mainly between and within the carbon fibers. Hence, the overall quality for HP1 is the lowest compared to the other plates. The sample made from the autoclave process AK1, shows a crack-free structure in resin and fibers. The large number of pores is conspicuous. The roundish shape of the pores indicates gas inclusions. The first sample from the RTM process, RTM-1, shows the micro structure with the least defects. The micro structure is dense and crack-free. The second RTM sample shows cracks within aramid and carbon fibers, as well as cracks propagating over matrix and fibers.

The figure 3-6 shows the C/C state of the samples after pyrolysis. For the hotpress sample typical block structure can be seen. The fiber matrix system is present within the carbon bundles. The sample manufactured from the autoclave process also shows the block structure which is typical for a strong fiber-matrix bond. Carbon blocks with carbon fiber as well as carbon blocks at the positions of the coked aramid fiber can be seen. The fiber structure of the converted aramid can still be seen.

Compared to HP1, the block structure is more defined. Matrix cracks occur transverse to the fiber direction and debonding. The RTM1 plate shows a structure similar to that of AK1. The fiber matrix blocks are also clearly visible. The structure appears more stretched and less dense than for AK1. RTM2 shows a distinct fiber split. The individual filaments are detached from the fiber composite. In conclusion, it can be said that the optical investigations coincide with the results from mercury porosimetry.

4. Material Characterization

To assess the final CMC materials, especially the acoustic properties are compared to their production efforts. However, the absorption characteristics of a porous material can be described by the the power loss of an acoustic wave, when traveling through a porous material Wagner et al. (2014). In order to assess the absorption properties of the CMC material the wall impedance, which describes the ability of the material to interact with its acoustic environment. The wall impedance of an homogeneous porous aborber of infinite thickness is therefore defined as

$$z_\infty = \rho c \frac{\sqrt{\kappa}}{\sigma} \sqrt{1 - j \frac{\Xi \sigma}{\omega \rho \kappa}} \tag{4-1}$$

by Möser (2009). The important factors in equation (4-1) for the characterization of an absorber material, are the porosity σ, length specific flow resistance Ξ and the structure factor κ.
The open porosity describes the ratio of accessible volume to total volume of the absorber material. In this work, the Archimedes method and mercury porosimetry are used to determine porosity.
Another important parameter for the absorber theory and for the assessment is the length specific flow resistance of the material. The length specific flow resistance describes the pressure drop across the material at a certain flow rate and is defined as

$$\Xi = \frac{\Delta p}{q_v} \frac{A_{sample}}{l_{sample}}, \tag{4-2}$$

where Δp is the pressure difference above the sample, q_v the volume flow rate, A the surface area and l the sample thickness. The measurements are carried out and evaluated in accordance with the European standard (DIN EN 29053). In Figure 4-1, the test setup is shown to determine the flow resistance. In order to minimize the leakage flow, the samples were galvanized with copper on their side surfaces and then soldered into a copper tube.

The microstructure of a porous absorber has a huge impact on the structure factor κ. The parameter describes the nature of the pore pathway inside the material in an indirect approximate way. It can derived from the acoustic performance of the absorber Wagner et al. (2014). However, comparing the microstructures and therefore the pore geometries of the materials, will lead to a better unterstanding of the structural factor. The determination of the pore size distribution can be done by mercury intrusion porosimetry. The pore size distribution can be calculated for mercury intrusion porosimetry by the Washburn equation Washburn (1921).

$$D = -\frac{4\gamma cos\theta}{p} \tag{4-3}$$

The equation(4-3) correlates the pore diameter of cylindrical shaped pores with the wetting of the pores by mercury through an applied pressure, with p as the applied pressure, γ the mercury surface tension and θ the contact angle. In addition scanning electron microscope (SEM) images are taken, to get an optical impression of the materials mircostructure.

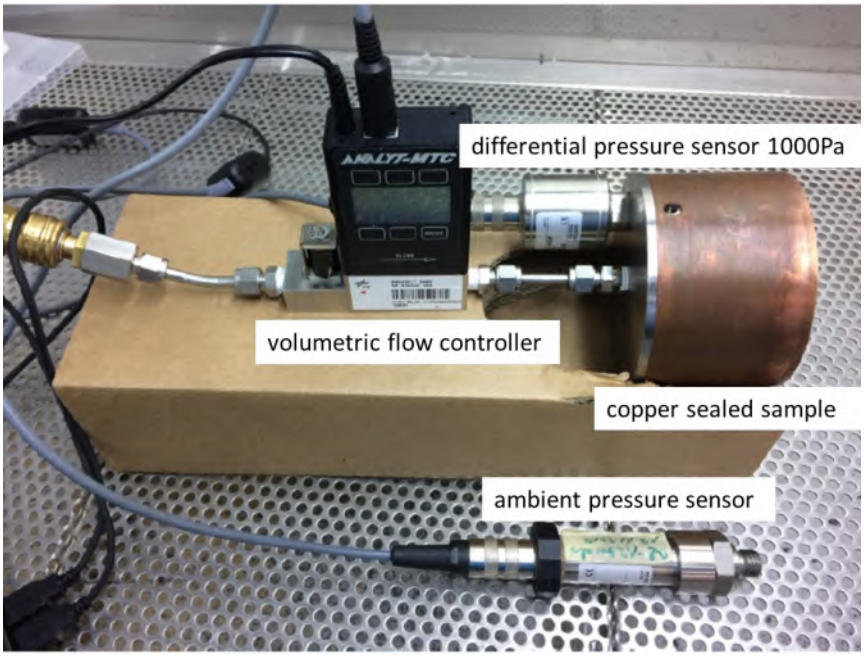

4-1 Test setup for the determination of the length specific flow resistance.

4.1. Porosimitry and Pore Size Determination

Before evaluating the results of the porous C/C-SiC plates, the **'classic' C/C** material will be reviewed once more. As already mentioned, the classic C/C is shown here for reference purposes only, as Wagner (2014a) has already confirmed the positive properties of the material.

The plate named **AK-1**, is the plate produced by the autoclave process. As for all the other materials, the pore distribution was also determined here. The figure 4-3 shows the pore distribution at the C/C intermediate state as well as in the final C/C-SiC state.

Particularly noticeable in the pore distribution is the fact that the pore distribution for the C/C state extends over a significantly larger pore diameter range. It can be seen that pores of $10^3 - 10^5\,nm$ are present in the material. However, the final siliconization mainly closes the small pores in the range of $10^3 - 10^4\,nm$, leaving pores in the order of $10^4 - 10^5\,nm$ in the C/C-SiC state. As shown in the Table 4-1, porosity decreases from 30.49% for the C/C to 15.78% for the final C/C-SiC. However, the porosity in the C/C-SiC state is comparable to the porosity of the classic C/C, as shown in Table

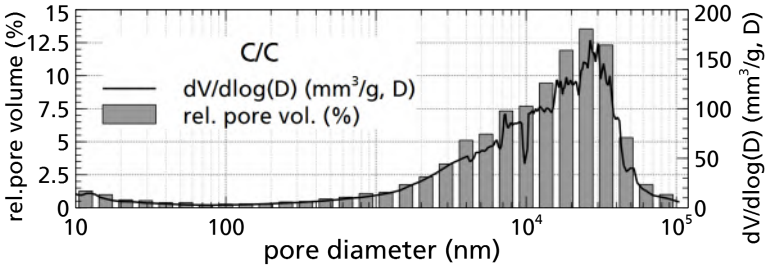

4-2 Measured pore size distribution for **C/C**.

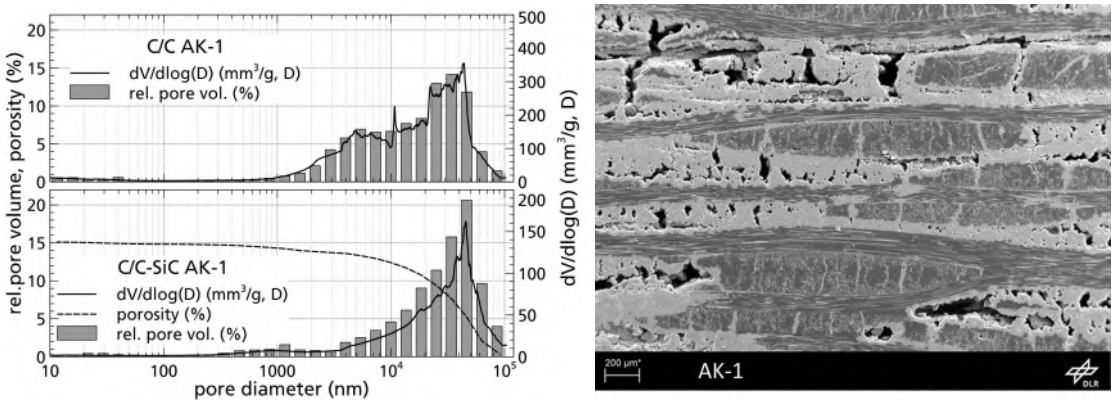

4-3 Pore size distribution of autoclave material at C/C and C/C-SiC (left) and SEM image of the final C/C-SiC (right).

4-1. Figure 4-3, right, shows a SEM image of the final C/C-SiC material. In the figure the resulting channel structure can be clearly seen, also the classic block structure, C-fiber blocks framed in SiC can be recognized in the figure.

Two plates are manufactured with resin transfer moulding **RTM**. For **RTM-1** a standard resin system was used but for **RTM-2** a micro porous resin in order to investigate the influence of the resin system on the properties of material. During characterization the RTM-1 plate showed very similar properties to the autoclave material. This can be seen if comparing the SEM images and pore distribution (Figures 4-4 and 4-3). In addition also the porosities are almost identical.

Furthermore, the RTM-2 material shows different properties compared to RTM-1, especially in the C/C state. The porosity of the RTM-2 material in the C/C state was measured with 44%. This is 3 times the porosity of the classic C/C. When examining the pore distribution, as shown in Figure 4-5, it can be seen that especially in the C/C state the pores are distributed very evenly in the range of $10^3 - 10^5\,nm$. For the final C/C-SiC, however, a similar behavior as for the other materials can be seen. The small pores are closed by siliconisation and only large pores in the range of $10^4 - 10^5\,nm$ are remaining. This becomes particularly apparent in the case of RTM-2 plate, as the porosity during siliconisation, as shown in Table 4-1, drops from 44% to 15%. This means that the final porosity is even below the value of the RTM-1 material. In the SEM image, Figure 4-5 (right), it is noticeable

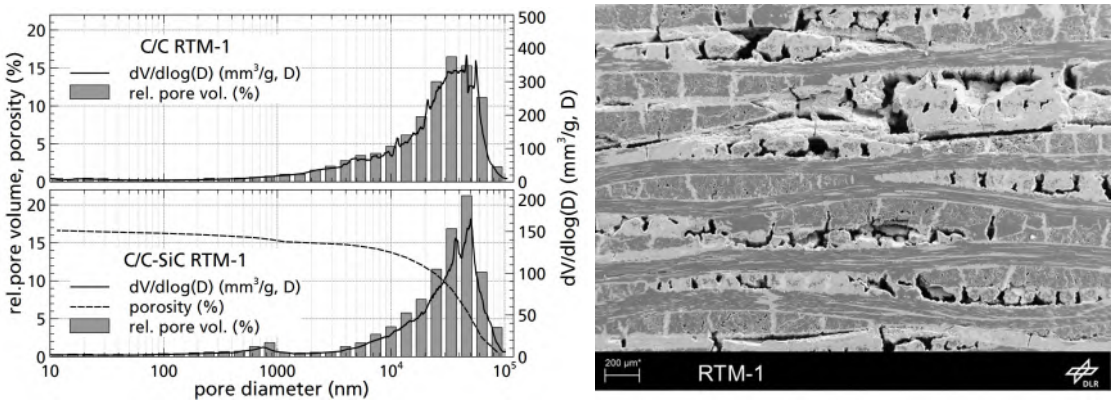

4-4 Pore size distribution of RTM-1 material at C/C and C/C-SiC (left) and SEM image of the final C/C-SiC (right).

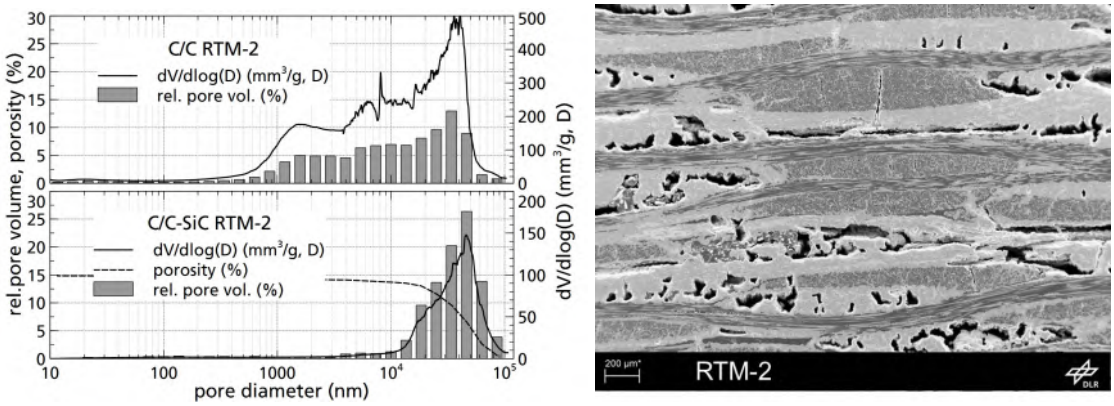

4-5 Pore size distribution of RTM-2 material at C/C and C/C-SiC (left) and SEM image of the final C/C-SiC (right).

that the typical block structure does not exist. The material looks more like a monolithic ceramic than a fiber-reinforced CMC material.

The **HP-1** material, as already mentioned, has been produced by hot pressing. Although the procedure is very simple in contrast to the other presented, the production of the plate turned out to be difficult. The handling of the material was particularly difficult during the C/C intermediate state. As shown in table 4-1, the porosity in the C/C state was measured to 44% and is thus similar to the C/C porosity of the RTM-2 material. However, the strength of the material was so low that no further samples could been cut out in the C/C state. After further processing to the final C/C-SiC material and the resulting reduction in porosity, the material could be characterized. With a final porosity of about 20%, HP-1 offers the highest porosity of all presented C/C-SiC materials. Especially the pore distribution, as shown in figure 4-6 shows a significantly different pore distribution than with the materials presented so far. Pore diameter here, is starting at $10^5\,nm$ and seems to increase. Unfortunately, measurements in this pore range cannot be determined with mercury porosimetry.

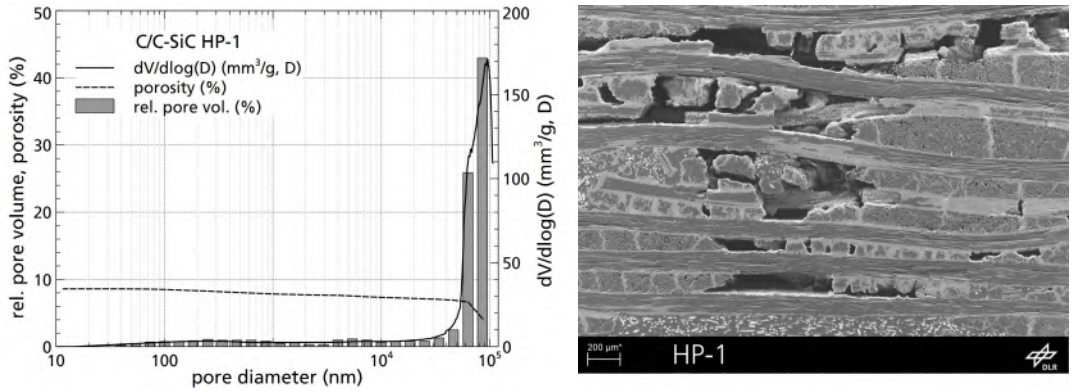

4-6 Pore size distribution for **HP-1** at final C/C-SiC state and SEM image.

4-1 Overview of porous properties in C/C and C/C-SiC compared to 'classic' C/C.

	peak pore Ø $[\mu m]$	**median pore** Ø $[\mu m]$	**porosity** $[\%]$	$\Xi\ [MPa\ s/m^2]$
'classic' C/C	29.95	13.92	14.98	25.72±0.13
AK 1 C/C	43.89	17.65	30.49±1.1	n/a
AK 1 C/C-SiC	45.55	29.48	15.78±0.43	7.49±0.05
RTM 1 C/C	46.208	26.376	30.47±1.09	n/a
RTM 1 C/C-SiC	50.595	31.33	17.52±0.75	4.94±0.059
RTM 2 C/C	35.925	11.045	44.20±0.83	n/a
RTM 2 C/C-SiC	45.8	36.75	15.26±0.38	11.65±0.06
HP 1 C/C-SiC	95.755	76.032	20.82	0.5144±0.002

Name	sample Ø [mm]	sample thickness [mm]
AK-1	91	29
HP-1	91	31.4
RTM-1	93	32.3
RTM-2	91	19.5
classic C/C	99.4	30

4-2 Sample dimensions for length specific flow resistance measurements.

4.2. Length Specific Flow Resistance

As mentioned, the classic C/C is shown here for reference purposes only, as Wagner (2014a) has already confirmed the positive properties of the material with regard to acoustic wave absorption. To qualify the set up for measuring the length specific flow resistance as shown in Figure 4-1 the C/C samples measured in Wagner et al. (2015) were measured again. Contrary to the first measurements, which showed a flow resistance of 13.3 $MPa\,s/m^2$, the current measurements show a significantly increased resistance of 25.72 $MPa\,s/m^2$, as shown in Figure 4-7. The major difference between the measurements can be explained by the fact that the samples were sealed much better in the current measurements. In contrast to the first measurements, the edge area of the samples was galvanized with copper and the samples were then soldered into the sample holder. This avoids possible leakage flow, whereby the pressure loss across the sample naturally increases significantly.

The length specific flow resistance measured for **AK-1** was measured with 7.49 $MPa\,s/m^2$ and is therefore significantly lower than the measured value for the classical C/C. The measured values are also shown in Figure 4-8. However, when measuring the length specific flow resistance, for the **RTM-1** material, Figure 4-8 showed even a lower result than the AK-1 material. When determining the length specific flow resistance for the **HP-1** material from the measured values, see figure 4-8,

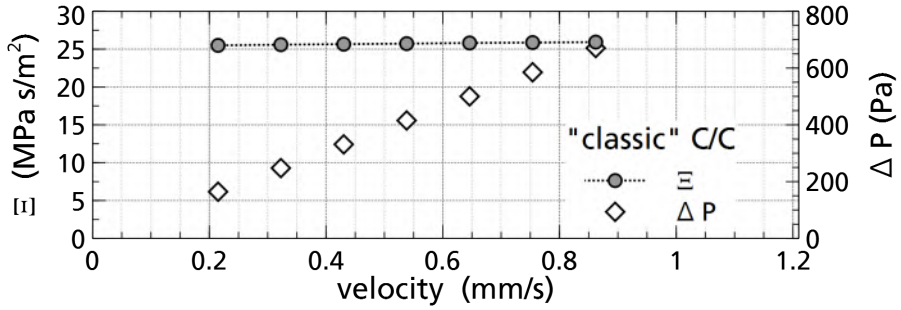

4-7 Measured length specific flow resistance for **C/C**.

the smallest measured flow resistance with only 0.5 $MPa\ s/m^2$ is obtained when processing the data.

Lately, the question has been raised again a number of times, how he length-specific flow resistance behaves at low pressures. Since the materials developed here are intended to damp the boundary layer during hypersonic flight, a typical ambient pressure that actually affects the material is somewhere around 12 hPa, assuming the altitude is around 40 km. Occurring shocks and Prandl-Meyer expansion at the vehicle changing pressures again.

In order to determine the influence of a low external pressure on the length specific flow resistance, additional measurements were carried out with the **'classic' C/C** and the for the HEG test campaign chosen **AK-1** material. Therefor a new test setup was used, as shown in Figure 4-9. The measurements were performed with the same samples as shown in Figure 4-1. In contrast to the original measurements, the measurements were conducted with nitrogen. In addition, due to the low pressures, pressure sensors were adapted with regards to the pressure range.

Figure 4-10 shows the calculated length specific flow resistances and the measured pressure loss over the sample starting from low pressure up to ambient pressure. On the x-axis the chamber or outlet pressure is plotted logarithmic. However, with both material measurements are performed with two different mass-flows. This has to be done, since outlet pressure and mass flow are the

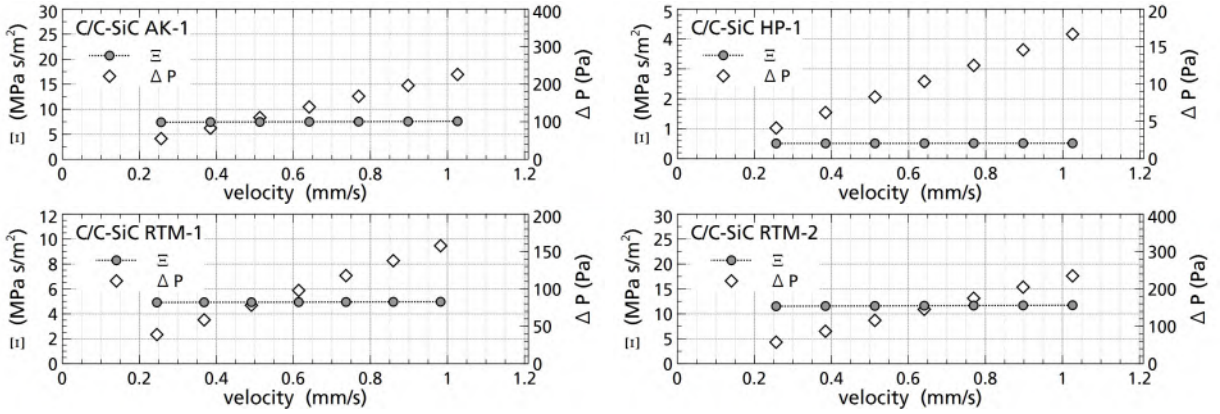

4-8 Measurements results for the length specific flow resistance.

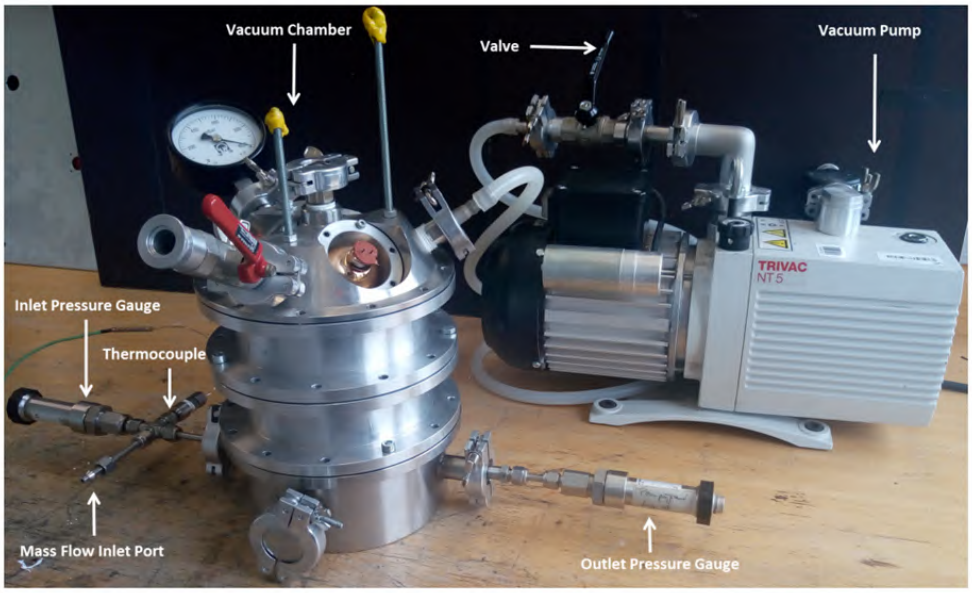

4-9 Adapted test setup for the determination of the length specific flow resistance under vacuum.

adjustable values and reservoir pressure was the free measured value. This means that flow velocity is changing with increasing outlet pressure and constant mass-flow. To ensure that the length specific flow resistance is not depending on the velocity, two mass-flows with one order of magnitude in between are chosen to perform the measurements. From the measurement at low pressures it can be seen in Figure 4-10, that the length specific flow resistance becoming significantly lower, but the pressure drop is significantly higher than for the ambient pressure measurement. This is mainly due to the fact that the same mass flows have been approached, but at low pressures the density is significantly lower and therefore the flow velocity significantly higher. This higher velocity results in a higher pressure loss according to Equation 4-2. From the Figure 4-10 it can also be seen, that

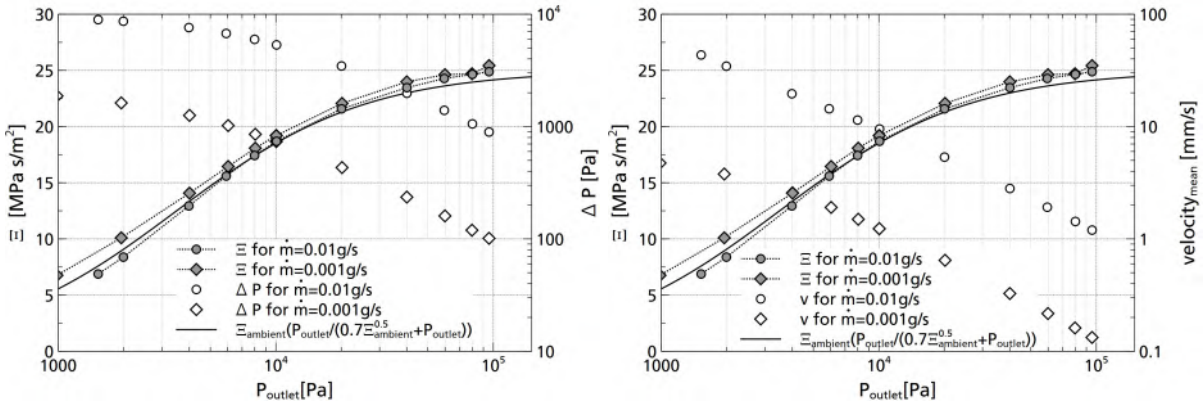

4-10 length specific flow resistance measured for 'classic' C/C under various vacuum pressures with δP and velocity influence.

with higher outlet pressure, the length specific flow resistance is approaching the length specific flow resistance obtained from the ambient measurement. In addition, a function was found which

reproduces the length-specific flow resistance only with the calculated ambient flow resistance and the outlet or ambient pressure, respectively, see equation 4-4.

$$\Xi_{vac} = \Xi_{amb} \frac{P_{out}}{0.7\Xi_{amb}^{0.5} + P_{out}}, \tag{4-4}$$

4.3. Surface Assessment

In addition to porosity measurement and the determination of the length specific flow resistance, the surface of the C/C and AK-1 was scanned for the first time with a 3D surface scanner, in order to give a first statement about the surface quality. Figure 4-11 summarizes the results of the C/C scan. What is noticeable here, is the dependence of the surface profile on the fiber orientation. Only very small fluctuations in the surface profile occur during the evaluation parallel to the fiber position. The resulting channel structure is clearly visible when evaluating the surface profile perpendicular to the fiber direction. It can therefore be assumed that the orientation to the incoming flow has an influence on the damping behavior. The surface was also scanned for the AK-1 plate. The results

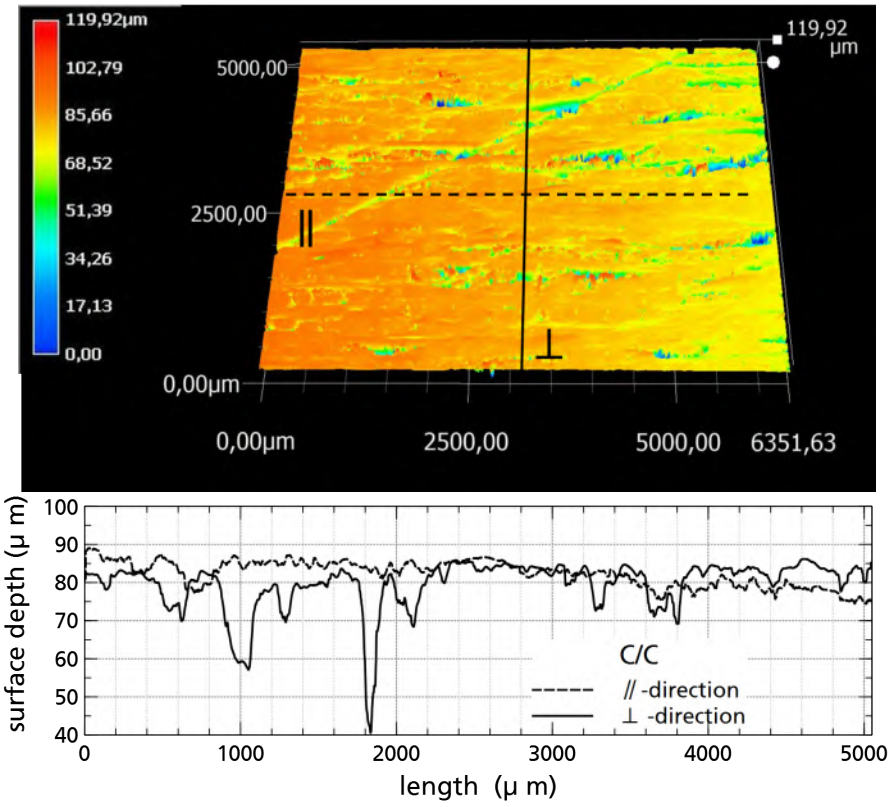

4-11 Measured surface profile for **C/C**.

are shown in the figure 4-12. Compared to C/C, it was found that this material has a much rougher surface for both fiber directions. After evaluation of the surface profile, it is recommended to align the sample for the final HEG test in the parallel fiber orientation to the flow.

However, a final assessment of the AK-1 surface was done by taking Computer Tomography scans. These scans, shown in Figure 4-13 are cutting planes showing the surface and then going in depth of the material. The result indicates that the surface roughness as measured in Figure4-12 is not a material property than rather a leftover from the mechanical machining. If large pores are clearly visible at the surface, they are almost completely disappeared within the first $0.5mm$. Nevertheless, this increased porosity at the surface can have a significant influence on the acoustic properties and must therefore be investigated further.

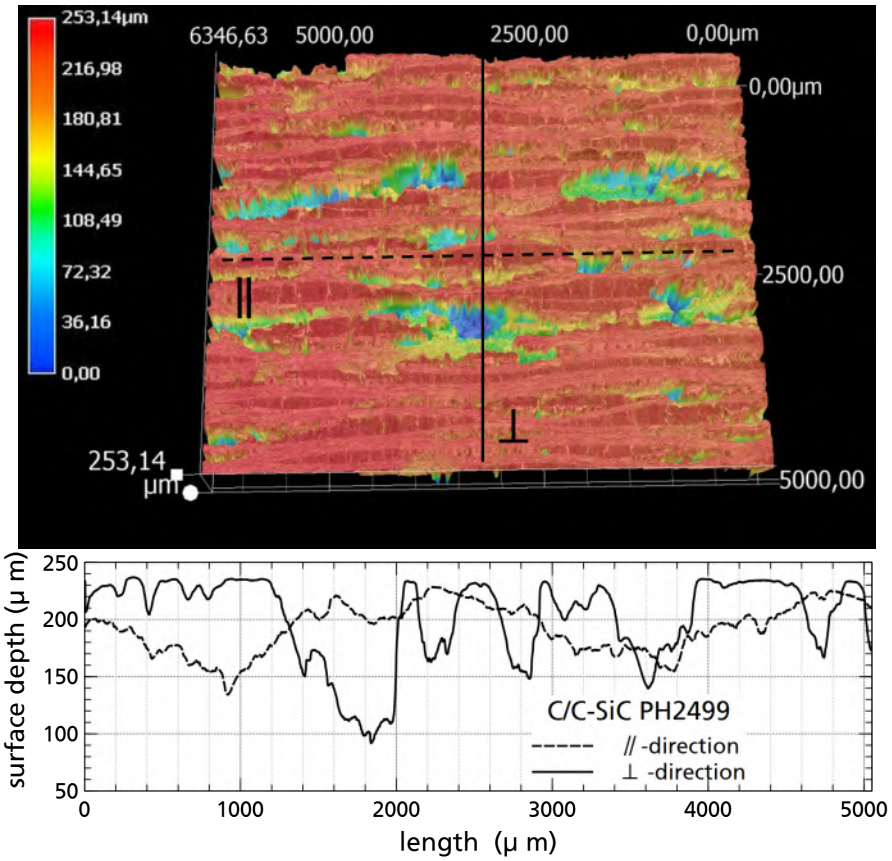

4-12 Measured surface profile for **AK-1**.

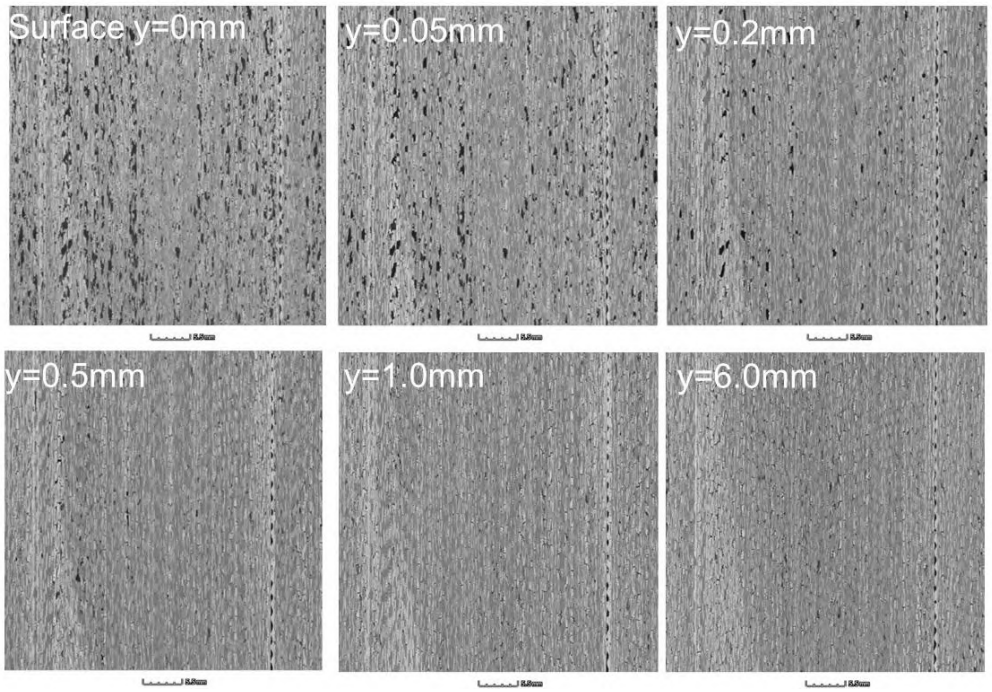

4-13 CT in depth images and porosity change of **AK-1**.

4.4. Reflection Coefficient Measurements

To assess the potential of the porous C/C-SiC with respect to transition control the requirement arises to determine the ultrasonic absorption characteristic at the surface. For this purpose a test rig was set up at DLR Göttingen to measure the reflection coefficient at varying static pressures as reported in Wagner et al. Wagner et al. (2014). The improved setup uses ultrasonic sound transducers covering a frequency range of 125 kHz to 490 kHz and thus include a wide range of the frequency domain of interest with respect to the second mode instabilities.

4.4.1. Qualitative Schlieren Measurements

A high-speed Schlieren setup (in a z-type shaped arrangement) is used to visualize the generated sound waves as they propagate towards the test sample from which they are reflected. The optical setup is illuminated by a Cavitar Cavilux Smart laser system, which is operated with a pulse width of 20 ns. A Phantom v2012 camera is used with a resolution of 640px x 480px at a frame rate of 70 kHz to capture the propagation of the sound waves. The exposure time limits motion blur to about 7 μm. Figure 4-14 depicts sound waves at different ultrasonic frequencies propagating along the transducer axis towards the investigates sample surface at the top of the image. The waves interact with the surface and are reflected back towards the receiver. The schlieren visualizations provide vital qualitative information, such as the dispersion angle of the sound waves, the point of interaction at the sample and the receiver and the wave dimensions. These information are required to numerically reconstruct the experiment. Unfortunately, the signal to noise ratio is too low to allow a quantitative evaluation of the wave amplitudes for instance.

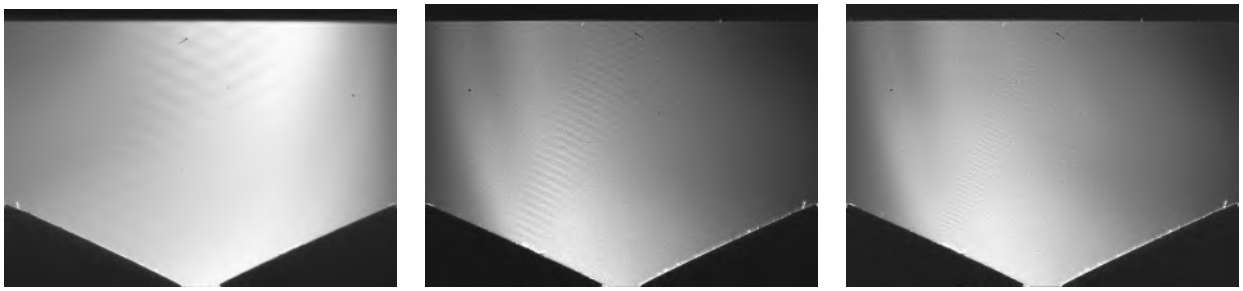

(a) f = 125 kHz (b) f = 300 kHz (c) f = 490 kHz

4-14 Schlieren visualizations of ultrasonic waves at 125 kHz, 300 kHz and 490 kHz at ambient pressure. Wave package generated by the transducer on the left.

Quantitative measurements beyond the Schlieren visualisation were investigated using an interferometric method introduced in the section 4.4.2.1.

4.4.2. Absorption Coefficient Measurements by means of Piezoelectric Sound Transducers

Ultrasonic air-coupled PZT[1] sound transducers with specific resonance frequencies were arranged pairwise to transmit ultrasonic wave packets towards a material sample of interest and to record

[1] Plumb-Zirconate-Titanate piezoelectric ceramic

the wave packet after its reflection from the surface. Sound transducers with resonance frequencies of 125 kHz, 289 kHz, 300 kHz, 405 kHz and 490 kHz were used at an angle of incidence of $30°$ and a distance of 40 mm such that the transducer axes intersect at the sample surface. Figure 4-15 shows a schematic of the setup while table 4-3 provides the geometric parameters introduced in the figure. The angle of incidence was chosen based on experimental work performed by Fedorov

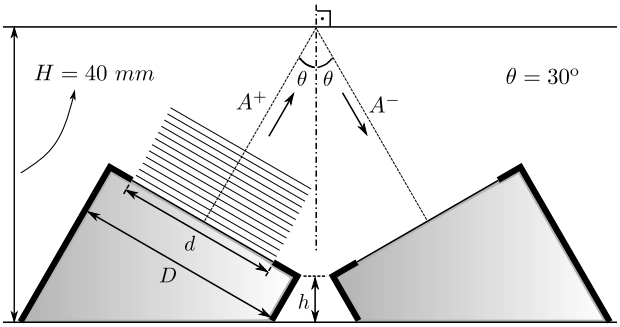

4-15 Schematic of the experimental setup using ultrasonic sound transducers - transmitter on the left, receiver on the right (not to scale).

et al. Fedorov et al. (2008). Further, it is justified by a numerical investigation conducted by Brès et al. Brès et al. (2010) showing that in all cases relevant for ultrasonically absorptive coatings the angle of incidence of second mode waves is smaller than $26°$. Further information on the experimental setup is provided in Wagner et al. Wagner et al. (2014), table 4-3 provides information on the sound transducer geometries.

$f\ [kHz]$	$d\ [mm]$	$D\ [mm]$	$h\ [mm]$
125	19	30	1
223	11	17	0
289	7	17	0.7
300	7	17	1
405	9	17	0
490	8	17	0

4-3 Geometric parameters of the transducer/receiver pairs.

Figure 4-16 provides the measured absorption coefficient of a sample. The absorption coefficient is provided as a function of pressure (to couple with a flight altitude) in a frequency range of 125 kHz to 490 kHz. The optimized setup allows conducting tests at pressures as low as approximately 2500 Pa. Note that the lowest pressure at which absorption measurements can be conducted depends on the sound wave frequency. The accessible low pressure range is of particular interest regarding possible applications of ultrasonically absorptive materials for transition control on hypersonic vehicles at flight conditions.

Figure 4-16 shows some important trends which were repeatably observed on various investigated porous materials:

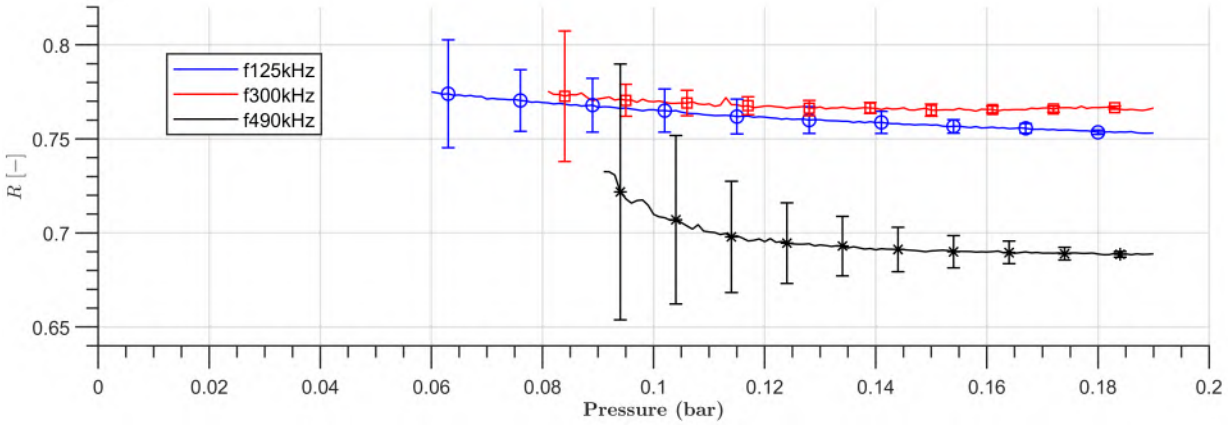

4-16 Directly measured reflections coefficient experimentally obtain on the final UAT material using sound transducers of different frequencies.

- a dependency on ambient pressure: the absorption coefficient decreases with decreasing ambient pressure, in particular in the low pressure range,
- a dependency on the frequency: the absorption coefficient increases with increasing frequency and
- with regard to the measurement technique: increasing uncertainties with decreasing ambient pressure.

The provided measurement errors are derived by evaluating a series of independent measurements with an acoustically hard surface. Since the reflection coefficient of that test case is known to be unity a mean, ambient pressure dependent, measurement error could be determined as indicated in figure 4-16. Note that this error does not account for inhomogeneous surface properties.

4.4.2.1. Quantitative Mach-Zehnder-Interferometer Measurements

In order to obtain complementary measurements to the one dimensional temporally resolved recording with the sound transducers an optical setup based on a Mach-Zehnder-Interferometer (MZI) built by Carl Zeiss in 1926 was implemented. The sound waves created by the PZT transducers are visualized and quantitatively evaluated based on interferometric measurements of the wave distribution. The experimental setup and measurements obtained with it will be described and the possibilities and challenges of this measurement technique when applied to the current experiments are discussed. A high speed camera in combination with the MZI is used to image the sound waves as they propagate towards the test sample. A schematic of the optical setup is given in figure 4-17. A green diode-pumped solide-state cw-laser (5320nm ,230mW) is used to illuminate the system. A non-resonant mode cleaning setup consisting of a focusing lens L1 = 20 mm and a pinhole P having a diameter of 20 μm is used to optimize and shape the beam profile of the laser. A second lens L3 = 40 mm expands the laser beam onto the forming lens L3 = 500 mm after which is becomes parallel. The parallel laser beam is then fed into the MZI. Here the laser beam is split into a reference path and the object path by means of two half mirrors (HM) and reflecting it with two full mirrors (FM). Both beams are collimated through the lens L3 = 500 mm and focused on the chip of the high speed camera, where they interfere. The high speed camera capturing the images is a Phantom

v2012, equipped with the FAST option, and is used at a resolution of 640x384px^2 and frame rate of 77kHz. The exposure time is set to the lowest possible value, which is 0.285 μs for the Phantom v2012. The time shift between the recording of consecutive images is 12.98 μs.

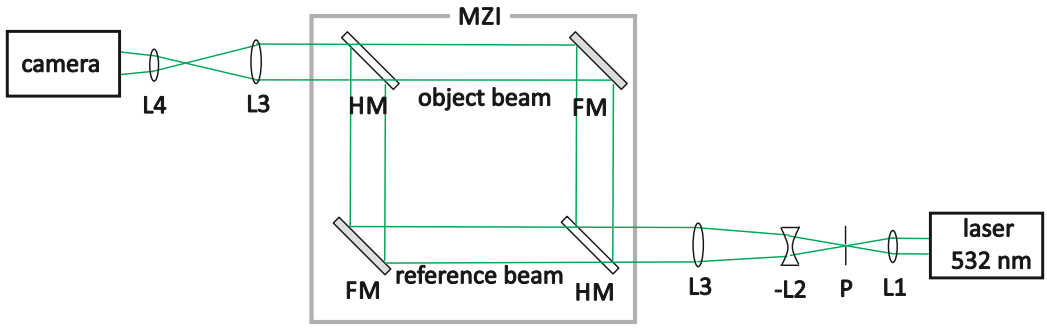

4-17 Schematic of the optical setup using a Mach-Zehnder-Interferometer (MZI). Non resonant mode cleaner (L1, P, -L2), main lenses (L3,L4), HM: half mirror and FM: full mirror are parts of the MZI.

The optical resolution of the system is determined with a 1951 USAF resolution test chart conforming to MIL-STD-150A standard (set by US Air Force in 1951) to be 198.43 μm (see figure 4-18b)). Transforming the frequency of f = 125 kHz used for the sound transducers at the current tests, we observe a wavelength of 2.74 mm. Therefore, we are able to resolve one wavelength with approximately 14 data points or pixels on the chip. A better resolution is not feasible, because of the limit of minimal exposure time of the camera, which introduces a motion blur of approximately 87 μm. Quantitative measurements of the pressure waves observed in the object beam of the MZI are based on the interference pattern formed by the superposition of light waves which originate from the coherent source of the laser but traverse different paths (object beam and reference beam, see figure 4-17). The fringe pattern indicates the local phase shifts arising from the difference in the optical paths traversed by the interfering beams.

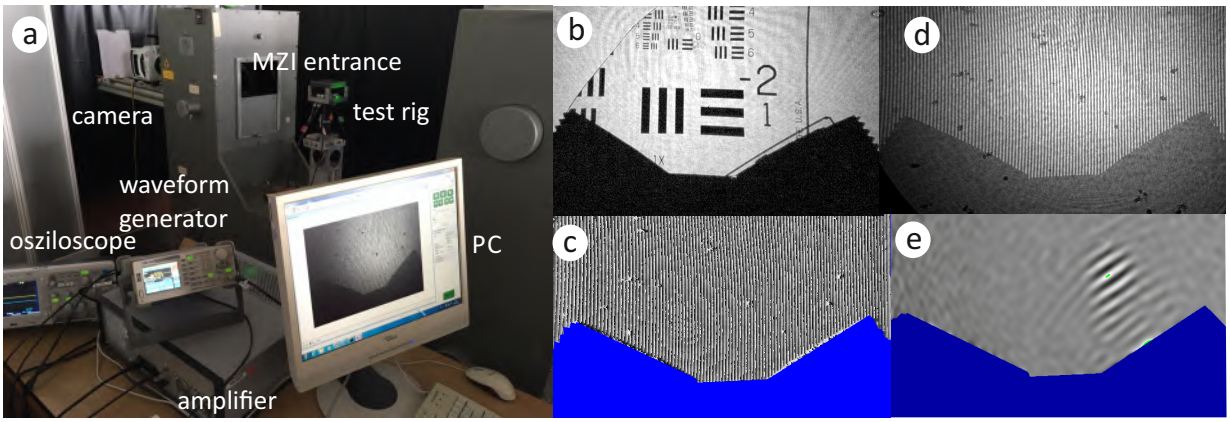

4-18 A photograph of the experimental setup is shown in a), a camera image of object beam with the optical resolution target is given in b). A typical interference pattern between the object and the reference beam without any phase change in the object beam is shown in d). The reconstructed interference pattern with a 2D-FFT is given in c) and the evaluated phase shift distribution of a wave packet in e).

The resulting interference pattern without any introduced phase change in the object beam can be controlled by adequate adjustment of the half and full mirrors of the MZI. In order to use a

two-dimensional Fast-Fourier-Transformation (2D-FFT) to evaluate the phase distribution from the interferograms, we create spatial carrier fringes as shown in figure 4-18d). The procedure is standard and well documented in the literature ((Kreis, 1996; Roddier and Roddier, 1987; Nakadate and Saito, 1985; Vest, 1979; Kujawinska, 1993)), therefore only a short summary is provided. The spatial intensity distribution of the fringe pattern, determined by the object beams phase shift Φ and the spatial carrier phase, can be written as

$$I(\vec{r}) = I_0(\vec{r}) + m(\vec{r})\cos(2\pi\nu_0(\vec{r})\vec{r} + \Phi(\vec{r})),$$

where I_0 and m are the background and contrast functions, ν_0 is the carrier frequency vector with components for the x- and y-direction and $\Phi(x, y)$ is the required phase function. If the largest gradient from the object phase is less than the spatial carrier phase and ν_0 is less than half of the sampling frequency Nyquist condition), then the phase distribution can be determined in both magnitude and sign. The above equation can be transformed into

$$I(\vec{r}) = I_0(\vec{r}) + c(\vec{r})e^{(2\pi i\nu_0\vec{r})} + c^*(\vec{r})e^{(-2\pi i\nu_0\vec{r})}$$

where

$$c(\vec{r}) = \frac{1}{2}m(\vec{r})e^{i\Phi}.$$

The superscript $(^*)$ denotes the complex conjugate. The Fourier transform of I(x,y) yields

$$\widehat{I}(\vec{r}) = \widehat{I}_0(\nu) + \widehat{c}(\nu - \nu_0) + \widehat{c}^*(-\nu - \nu_0).$$

This clearly reveals the purpose of generating the fringe carrier system: Disturbing changes in background intensity I_0 are of lower frequencies. By applying a comparable high carrier frequency ν_0, the information of the fringe system is separated from the disturbing low frequencies in the Fourier domain, shifting it to the vicinity of ν_0. The determination of the phase distribution $\Phi(r)$ is straight forward. First the domain $c(\nu - \nu_0)$ of the interferogram around the carrier frequency is determined via the FFT, then all frequencies outside this domain are set to zero. Then the domain centered around ν_0 is transferred towards the origin (zero-frequency), which removes the carrier. This resulting frequency field is the inverse Fourier transformed yielding $c(r)$. Finally the phase modulo 2π (see figure 4-18e)) is calculated by

$$\Phi(\vec{r}) = \arctan\left(\frac{Im(c(\vec{r}))}{Re(c(\vec{r}))}\right).$$

A first result of the observed waves is given in figure 4-19. The test rig was installed without a reflective surface in the object beam of the MZI. A wave packet with a frequency of f = 125 kHz was generated with 4 periods. The image sequences given in 4-19 show the temporal and spatial two dimensional evolution of the wave packet generated by the sound transducers. The propagation of the wave packet can clearly be observed and the spatial broadening perpendicular to the direction

of motion can be determined. The first recording at t = 12.98 μs shows the appearance of two waves (1/f = 1/125 kHz = 6 μs), one image later, the complete packet (4 periods) is visible. As the packet travels along the propagation direction, it can be observed that additional weak waves are emitted behind the wave packet. This is due to the decay of the transducer.

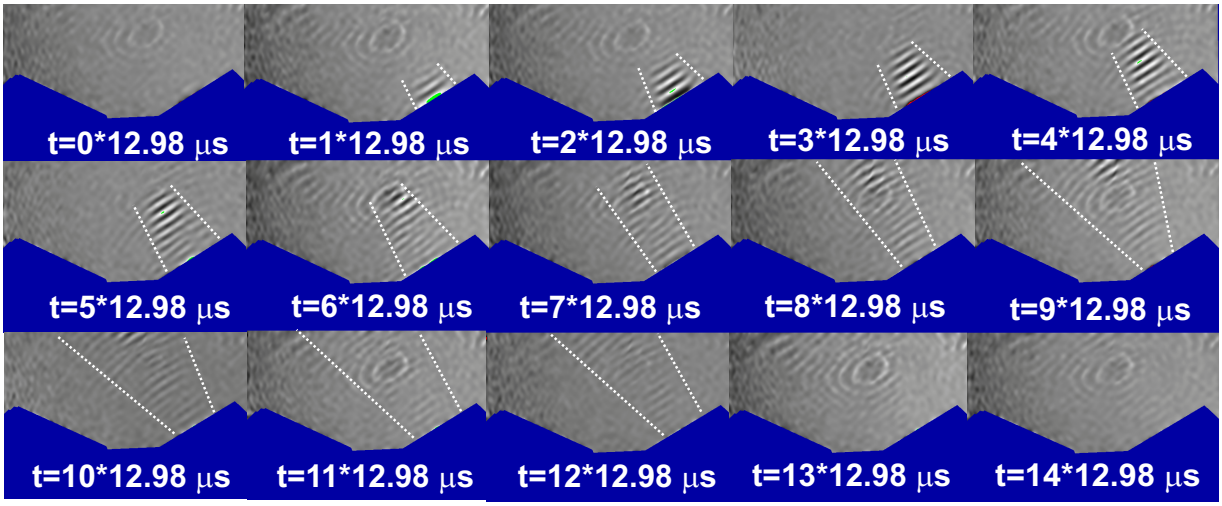

4-19 Temporal and spatial evolution of the sound waves. The test rig is used without a reflective wall.

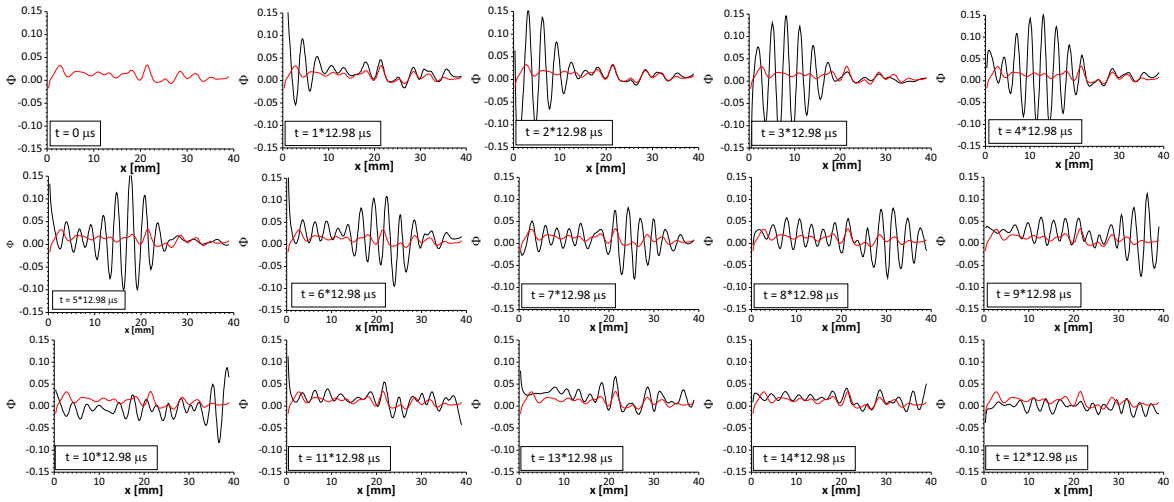

4-20 Temporal evolution of the sound waves along the symmetry line of the propagation direction. The red curve is the reference recording at t = 0 μs. The test rig is installed without a reflective plate.

In figure 4-20 the phase data along the symmetry line of the propagation direction is shown for different instants in time. The data is extracted from the images shown in 4-19. For reference purposes, the data at t = 0 μs is added to every graph as a red line. The propagation and damping of the wave packet over time can be observed until it leaves the field of view. We note at this point, that the signal to noise ratio is approximately 5 in average over all data obtained. To improve this ratio, the measurements can only be performed in a different gas than air, which would yield stronger signals. To investigate how far the analysis of the data can be driven, a set of 10 consecutive

recordings of a continuous generated waves of f = 125 kHz are spatially averaged. We compare the averaged data of the incoming and the reflected waves in figure 4-21 for a solid wall and a porous wall.

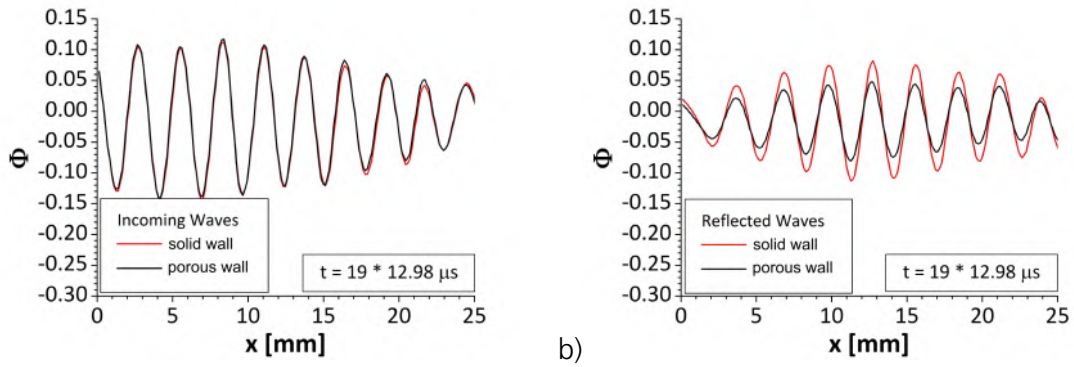

4-21 Wave distribution of incoming waves and reflect waves for different surfaces.

The data in figure 4-21a) compares the recorded waves approaching the walls (incoming waves). The repeatability for the different experiments is very good. The comparison for the waves which return from the walls after reflection (reflected waves) in figure 4-21b) reveals the differences of both waves after the reflection at the solid and the porous wall. The amplitude is obviously lower, but a distinct phase shift cannot be observed.

It could be shown that Mach-Zehnder-Interferometer measurements can be used to directly visualize and quantify the ultrasonic waves emitted towards and reflected by the surface. However, in the course of the project only transducer based measurements of the sound absorption were used.

5. Wind Tunnel Testing

5.1. Wind Tunnel Model Design

5.1.1. Layout

Starting in February 2018 the wind tunnel model requirements document was generated in an iterative process considering aerodynamic, acoustic, material and manufacturing requirements. The final version of the document was used for the invitation to tender which was sent out to a number of external contractors in July 2018. The decision to assign the design of the model to an external contractor was mainly motivated to save time. The contract was finally assigned to the DEHARDE GmbH, a company we already had good experience with, in early August 2018. The design process was concluded at the end of the second reporting period except some minor changes regarding the instrumentation. The design process lead to an adaptation of the existing base body and a complete

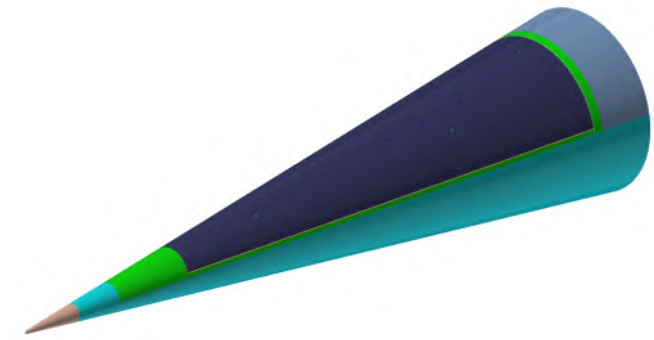

(a) a

(b) b

5-1 CAD drawing of the complete UAT wind tunnel model and the new model insert. Total model length is 1.1 m.

redesign of an insert carrying the porous ceramic. The complete model is depicted in figure 5-1a.

The insert carrying the CC-SiC is shown in figure 5-1b. The ceramic elements are carried by an aluminum frame which is fitted to the main frame of the model. The insert is designed such that it can be prepared and instrumented independently from the rest of the model to reduce the preparation time prior to the test campaign.

Figure 5-2a shows the rear of the insert as well a vertical cut through it, figure 5-2b. The present design considers the lessons learnt in previous studies with similar models. For instance the mechanism to firmly fix the insert in the base model was changed to assure a repeatable pulling force to fix the insert in the model. Furthermore, to improve the positioning of the insert guiding bolts were included in the design. The insert frame supports the porous ceramic using a frame structure beneath the ceramic while access to the instrumented sections is granted. Additionally, the

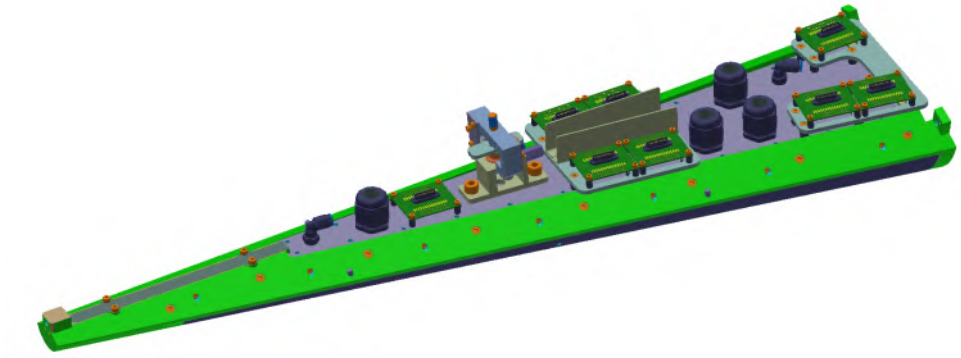

(a) rear view

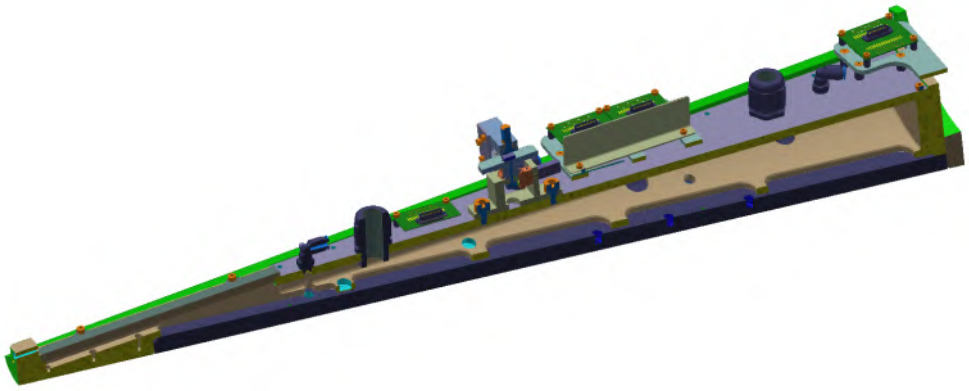

(b) vertical cut

5-2 CAD drawing showing the model insert from behind an in a section view.

insert is air tight to control the pressure behind the porous material and the gas species inside the porous absorber. Thus, the design provides two additional parameters to investigate the ultrasonic absorption capabilities of the CC-SiC using different back pressures or a different medium.

5.1.2. Insert Length Optimization

This subsection addresses a possible reduction of the insert length for the C/C-SiC insert. The pre-analysis is based on an experiment with a similar cone geometry, which has the same dimensions as in the present project: a $7°$ half-angle blunted cone with a nose radius of $2.5\,\mathrm{mm}$ and a total length of about $1\,\mathrm{m}$. An experimental test case with an unit Reynolds number of $Re_\mathrm{m} = 6.4 \times 10^6/\mathrm{m}$ and a Mach number with 7.5 is chosen. For the LST transition prediction the semi-empirical approach of the e^N-method is applied. In figure 5-3 the results of the smooth surface side, marked by black lines, are visible: The measured transition x-coordinate are from a previous wind tunnel test campaign of the HEG (see Wagner et al. Wagner (2014b); Wartemann et al. (2015)). The measured $x_\mathrm{trans,smooth}$ results in a $N_\mathrm{trans,smooth}$ of about 8.4. This N-factor is used for the following analysis.

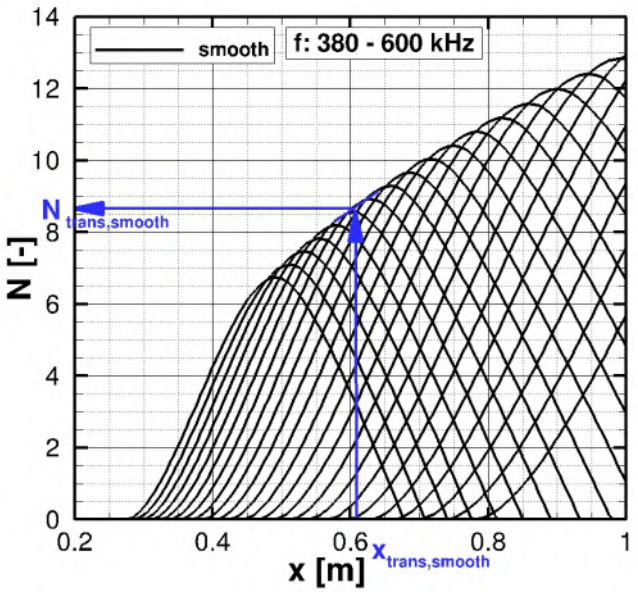

5-3 Semi-empirical approach of the e^N-method, $Re_\mathrm{m} = 6.4 \times 10^6/\mathrm{m}$.

Figure 5-4 shows the investigations for the reduction of the insert length: black lines mark the results for the smooth cone and red lines are standing for a cone with porous material from $182mm$ up to $1000mm$, which is the maximal possible insert length. Additionally, the N-factor distributions for an insert length of $400mm$ up to $1000mm$ is visible in fig. 5-4.a (blue lines) and ranging from $500mm$ up to $1000mm$ in fig. 5-4.b (orange lines). Only at the beginning of the cone differences are visible due to the variation of the insert beginning. In the rear of the cone, the distributions merge. This results in the same predicted transition start of about $0.85m$. The reason for this behavior is given in figure 5-5.a, which shows the results of an insert ranging from 600 mm up to 1000 mm (green lines). Applying a boundary condition for the porous material, the chosen LST approach results in an abrupt change of the growth rates at the beginning of the insert (figure 5-5.a). Thus calculations based on PSE would be preferable. Nevertheless, the analysis can be used as trend. The shorter selected insert length of fig. 5-5.b (green lines) results in a different predicted

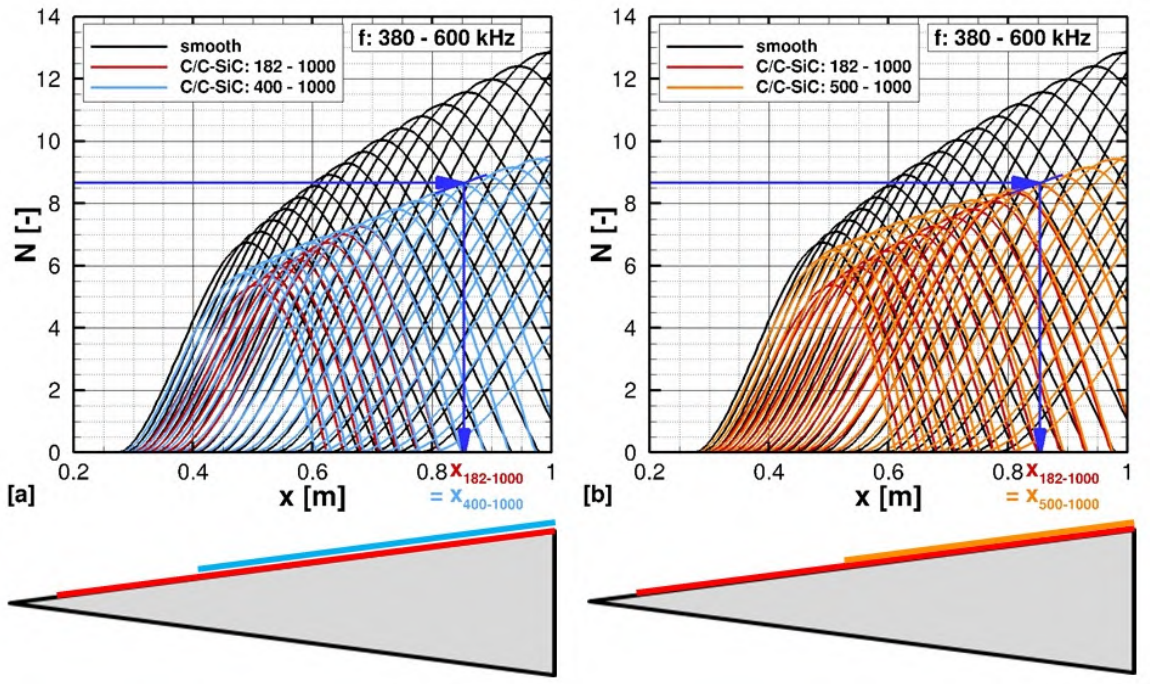

5-4 Variation of the insert length: $400mm$ - $1000mm$ (blue lines), $500mm$ - $1000mm$ (orange lines), $Re_{\mathrm{m}} = 6.4 \times 10^6/\mathrm{m}$.

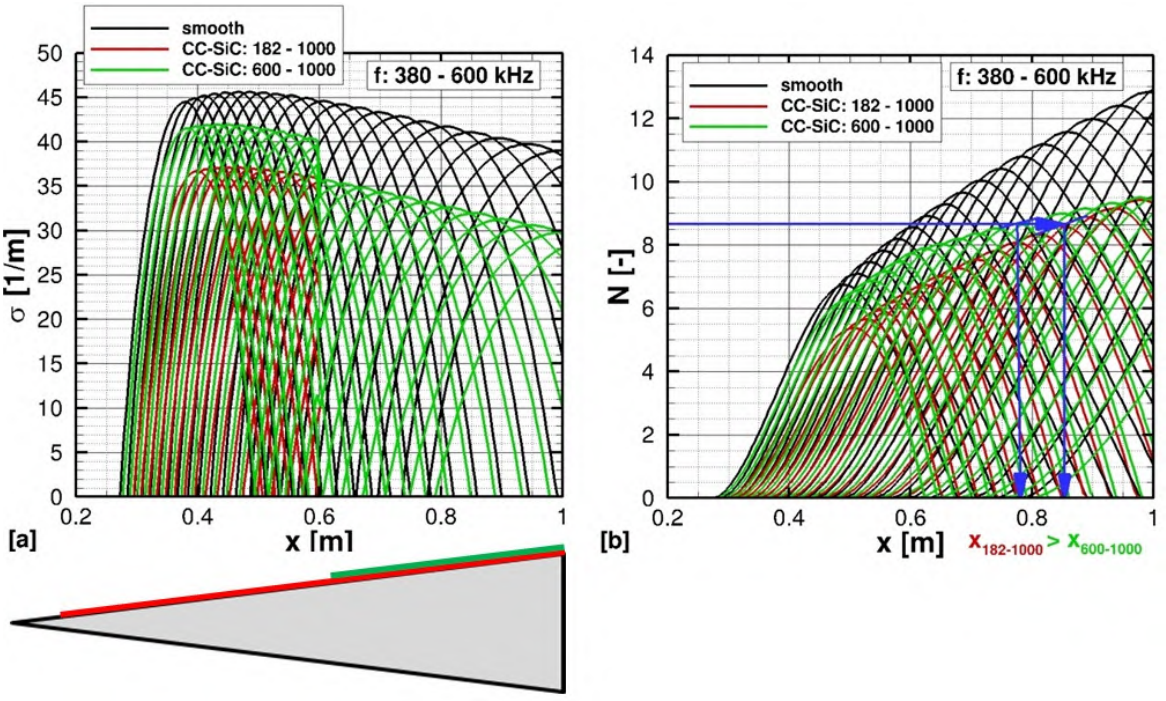

5-5 Variation of the insert length: $600mm$ - $1000mm$ (green lines), $Re_{\mathrm{m}} = 6.4 \times 10^6/\mathrm{m}$.

transition beginning, compared with a porous insert over almost the whole cone (red lines). To be on the safety side, the numerical recommendation for the start of the insert is $x \leq 500\mathrm{mm}$, which delivers the same predicted transition start as an insert with maximal insert length for the investigated Reynolds number. For the HEG test campaign different free stream conditions with varied unit Reynolds number were planned / performed, thus finally an insert with a starting x of $305mm$ is chosen. This reduced insert length should offer a sufficient effectiveness for the whole selected Reynolds number range.

5.1.3. Instrumentation

The model instrumentation consists of surface thermocouples (Type E) to measure the surface temperature over time and thus to derive the surface heat flux. Furthermore, the model is equipped with pressure transducers (KULITE) to resolve the static surface pressure for angle of attack and yaw angle cross-checks. Dedicated high speed transducers (PCB and ALTP) are used to measure surface pressure and surface heat flux fluctuations which can be correlated to the second mode instability. In addition to the surface mounted transducers temperature sensitive paint was applied to visualize the surface temperature distribution with a greatly improved spatial resolution.

Figure 5-6 shows the dimensions of the model and the CC-SiC insert, which starts 300 mm downstream the sharp model tip. The sketch also shows the principle transducer locations around the cone to which will be referred in section 5.3.

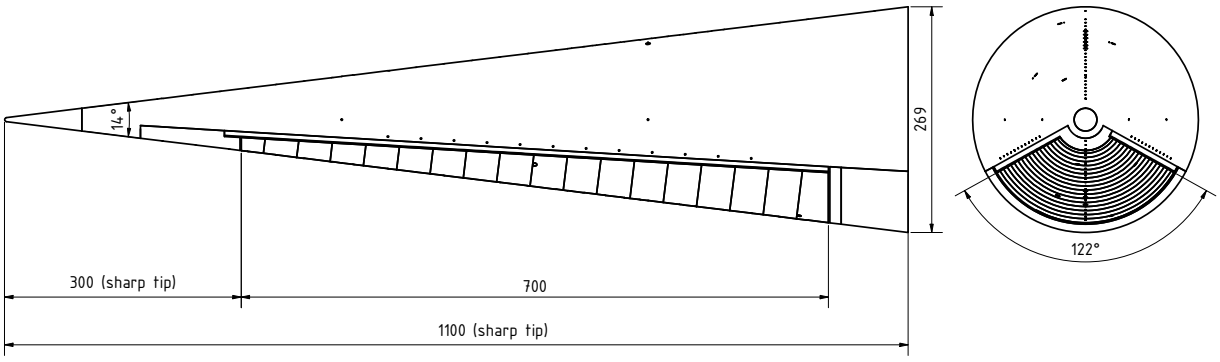

5-6 Sketch of the wind tunnel model holding the porous CC-SiC insert starting 300 mm downstream the sharp model tip.

5.2. The High Enthalpy Shock Tunnel Göttingen (HEG)

The experimental results presented in this paper were obtained at the High Enthalpy Shock Tunnel Göttingen (HEG) which is a free-piston driven reflected shock tunnel depicted in figure 5-7. It

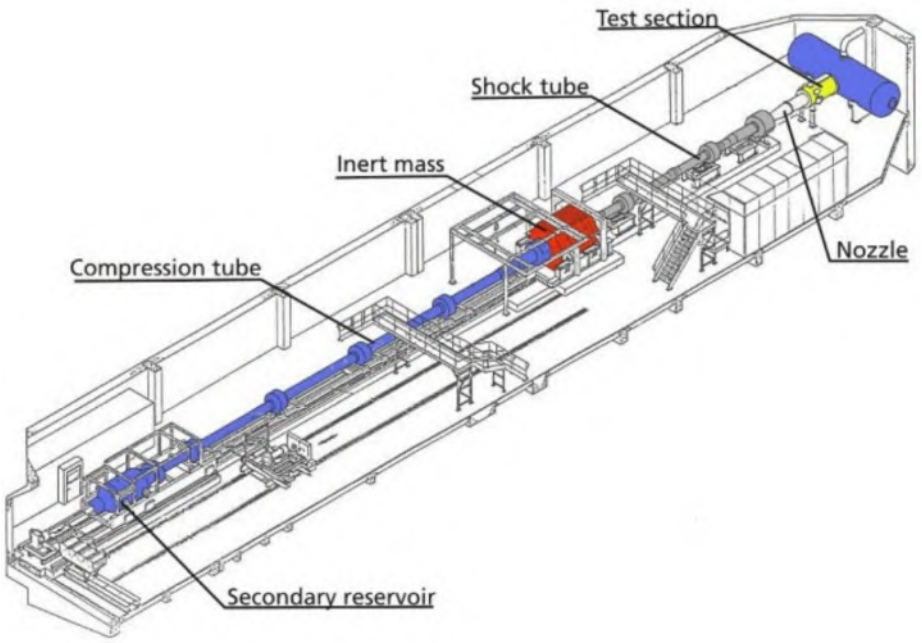

5-7 Schematic of the HEG facility used for experiments.

provides a pulse of gas to a hypersonic nozzle at stagnation pressures of up to 200 MPa and stagnation enthalpies of up to 25 MJ/kg.Eitelberg et al. (1992); Eitelberg (1994) Its range of operating conditions was successively extended to allow investigations of the flow past hypersonic flight configurations from low altitude Mach 6 up to Mach 10 at approximately 33 km altitude.Deutsches Zentrum für Luft - und Raumfahrt (DLR) (2018) In the present study HEG was operated at Mach 7 using a nozzle exit diameter of 0.59 m and an expansion ratio of 218. The nominal test conditions used in the present study are listed in table 5-1.

Condition	H3.4R1.6	H3.5R2.4	H3.2R4.1	H3.0R6.4	H9.8R2.2
$p_0\ [MPa]$	8.0	12.7	19.2	28.4	44.1
$T_0\ [K]$	2810	2895	2734	2582	5935
$h_0\ [MJ/kg]$	3.4	3.5	3.2	3.0	9.8
M_∞ [-]	7.4	7.3	7.4	7.4	6.2
$T_\infty\ [K]$	277	285	268	248	1084
$\rho_\infty\ [g/m^3]$	11.0	17.7	27.6	43.2	23.5
$u_\infty\ [m/s]$	2450	2480	2422	2350	4036
$Re_m\ [1/m]$	$1.6 \cdot 10^6$	$2.4 \cdot 10^6$	$4.1 \cdot 10^6$	$6.4 \cdot 10^6$	$2.2 \cdot 10^6$

5-1 Selected nominal operating conditions of HEG at M = 7.4.

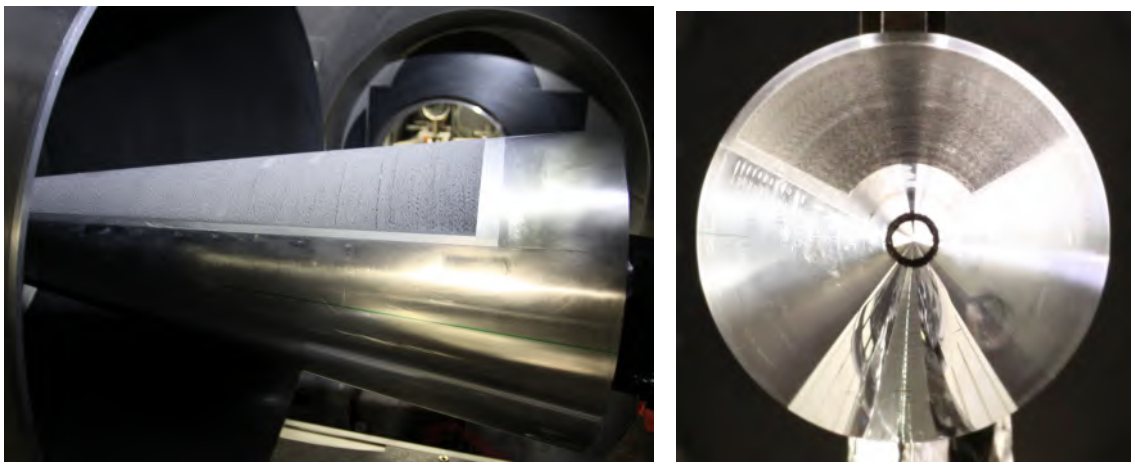

(a) Test section view. (b) View through nozzle.

5-8 Wind tunnel model mounted in the test section of HEG.

5.3. Experimental Results

The preceding efforts concluded in tests on a generic 7 degree half-angle cone with a highly polished surface and an insert of the porous, temperature stable C/C-SiC as depicted in figure 5-6. Each test provided results on the solid surface and the porous surface at the same time allowing to directly compare the effect of the absorber on the second mode dominated transition process.

In the course of the interpretation of the results it should be kept in mind that the maximum observable transition delay is limited in the present setup. This is due to the fact that an early transitioned boundary layer on the solid surface will eventually *contaminate* the laminar boundary layer above the porous surface due to its lateral spread.

Figure 5-9 shows a schematic of the cone model together with a simultaneous high speed schlieren visualization of the boundary layer of the solid and the porous wall. The test condition corresponds to H3.2R4.1 as detailed in table 5-1 and the nose bluntness is 2.5 mm. The boundary layer state is clearly different on both sides of the cone. A thick boundary layer with a rich set of turbulent structures is well visible above the solid surface of the cone indicating a fully turbulent boundary layer. In contrary, the boundary layer on the porous surface is thin, shows no turbulent structures, and thus is fully laminar. The observation is complemented with the heat flux distribution provided in figure 5-12 which confirms the above interpretation.

The subsequent figures provide normalized surface heat flux distributions which indicate the laminar-turbulent transition location on the surface. The nose radius has a significant impact on the boundary layer stability along the cone and thus has an impact on the absorber effect. Therefore, the results are grouped accordingly.
Figure 5-10 provides the results for the smallest nose tip. The open square symbols correspond to the solid surface while the full circles correspond to porous C/C-SiC surface. Furthermore, the

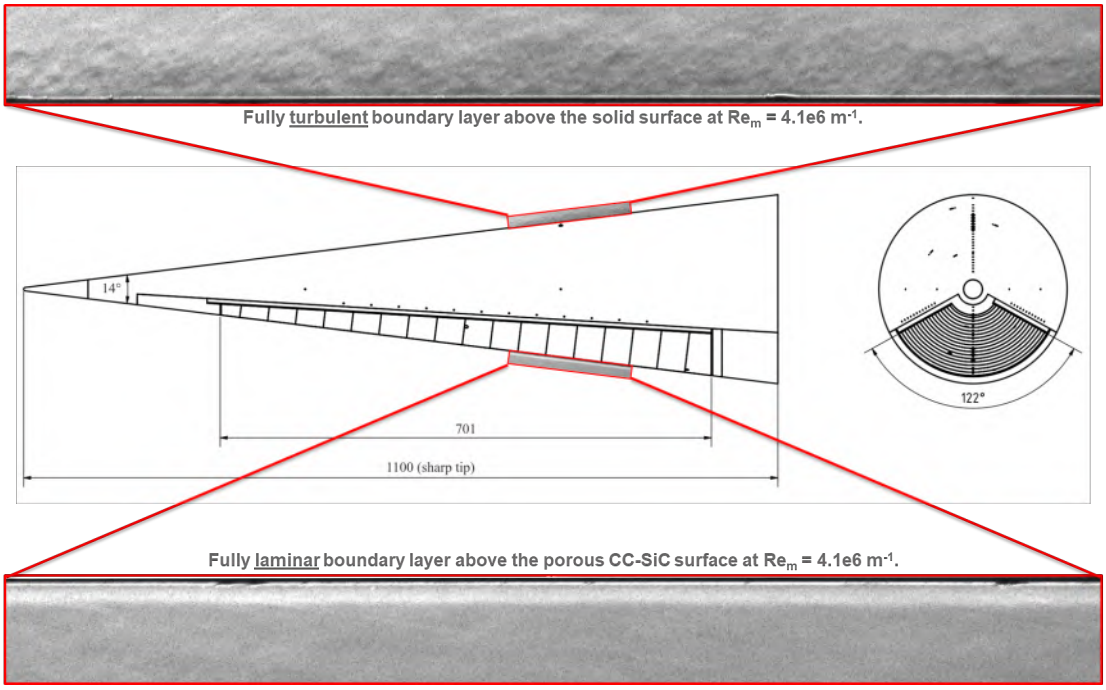

5-9 Schlieren visualization on the cone. Top: solid surface, Botton: porous C/C-SiC. Nose radius 2.5 mm.

most upstream extent of the insert is indicated in the figure, $\approx 0.3\,\mathrm{m}$. It can be seen that for the highest unit Reynolds number of $6.4 \times 10^6\,\mathrm{m}^{-1}$ the transition location on the solid and the porous surface are almost identical since the instability growth largely takes place upstream of the insert. For lower unit Reynolds numbers a significant transition delay is observed on the C/C-SiC surface. At the present test condition boundary layer transition could be fully suppressed for unit Reynolds numbers below $2.4 \times 10^6\,\mathrm{m}^{-1}$.

Stabilizing the boundary layer using a slightly increased nose bluntness leads to the heat flux dis-

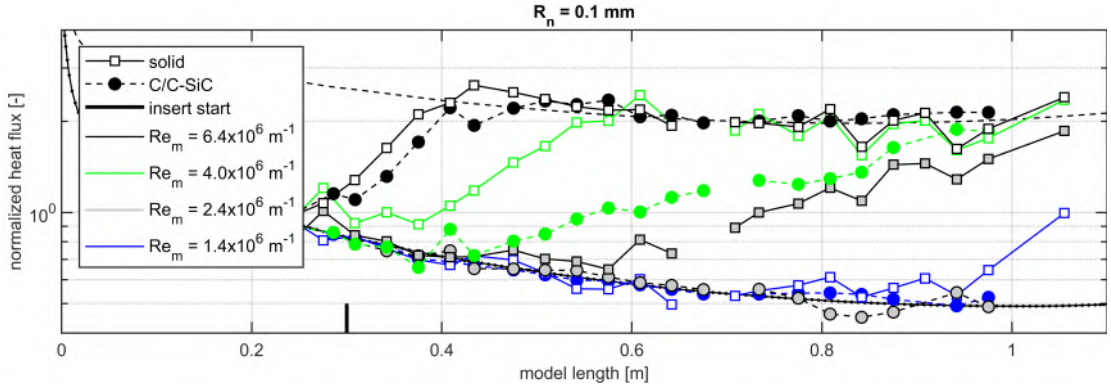

5-10 Normalized surface heat flux density on solid and porous cone surfaces for various Reynolds numbers and a nose radius of 0.1 mm.

tribution shown in figure 5-11. For the highest unit Reynolds number still both transition locations remain identical as most of the transition process takes place upstream of the porous insert. For a lower unit Reynolds number of about $4.0 \times 10^6\,\mathrm{m}^{-1}$ the start of transition on the solid surface

is observed at a Reynolds number of 1.5×10^6, corresponding to 0.375 m downstream the tip. In contrast, on the porous surface the start of transition can be observed around 0.7 m from the tip corresponding to about 2.8×10^6 in terms of local Reynolds number. Thus, the critical Reynolds number was almost doubled on the absorber side. The local surface heat flux in the present case did not reach the fully turbulent level before the end of the model. For lower unit Reynolds numbers transition on the porous surface was fully suppressed.

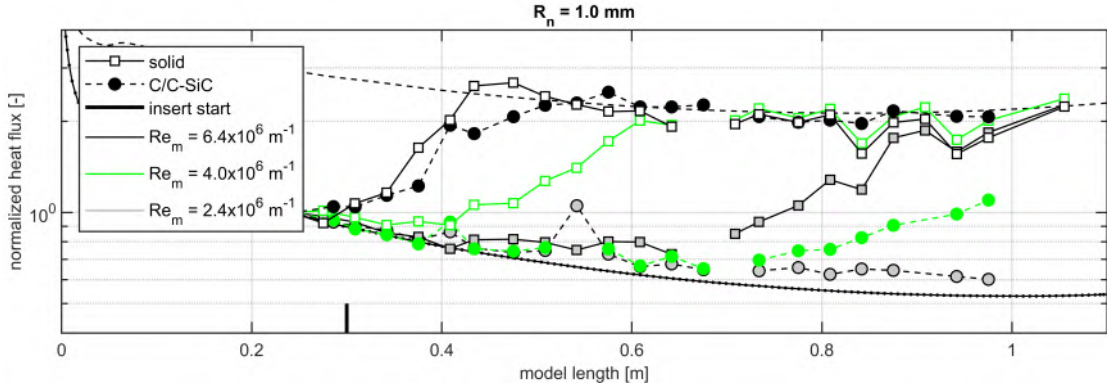

5-11 Normalized surface heat flux density on solid and porous cone surfaces for various Reynolds numbers and a nose radius on 1.0 mm.

Figure 5-12 provides the heat flux distributions for of nose radius of 2.5 mm as used in the HIFiRE 1 flight test. In addition to the new C/C-SiC data the heat flux distribution measured on the originally used C/C material is provided, see open triangles. This allows to compare the performance of both absorber types at the same nominal test condition.

The boundary layer is again stabilized by the increased model bluntness, as expected. For the highest unit Reynolds number of $6.4 \times 10^6\ \mathrm{m}^{-1}$ a strong transition delay above the C/C-SiC is observed where the surface heat flux does not reach the fully turbulent level before the end of the model is reached. As seen in the figure the absorber performance could be significantly increased compared to the original C/C. **For all lower unit Reynolds numbers the boundary layer above the C/C-**

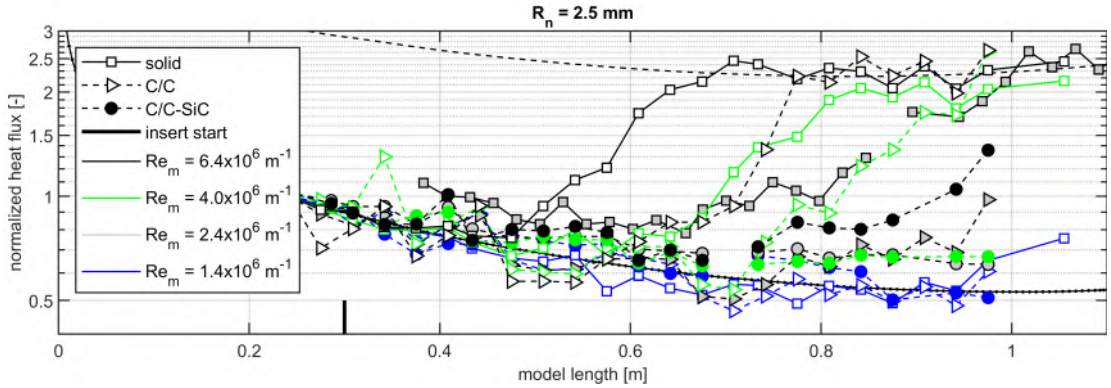

5-12 Normalized surface heat flux density on solid and porous cone surfaces for various Reynolds numbers and a nose radius on 2.5 mm.

SiC remains fully laminar! Again it can be shown that the C/C-SiC absorber works more efficiently than the C/C absorber.

Finally, for the largest nose bluntness of 5 mm, and thus the most stable boundary layer, the fully turbulent heat flux level is not reached in the investigated Reynolds number range, see figure 5-13. For better readability the data gathered on the C/C surface are not shown in the figure. It interesting to note that for the unit Reynolds numbers above $2.4 \times 10^6\ \mathrm{m}^{-1}$ the surface heat flux on the porous surface does not completely follow the predicted laminar trend. Even though, the boundary layer does not transition yet, the surface heat flux rises above the laminar level whereas the heat flux distribution shows a comparable trend in the two highest unit Reynolds number cases. The cause for that observation is not clear yet and needs further investigation.

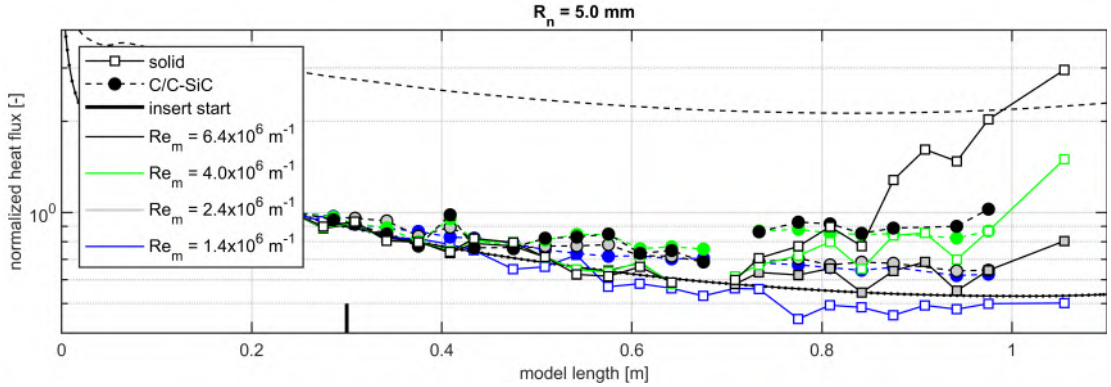

5-13 Normalized surface heat flux density on solid and porous cone surfaces for various Reynolds numbers and a nose radius on 5.0 mm.

Throughout the tests surface mounted transducers, FLDI and High Speed Schlieren was used to measure 2nd mode instabilities in the boundary layer above the absorber. Unfortunately, (from an experimentalists point of view only) the absorber was so effective in damping the instability waves that no information could be extracted to allow a quantitative analysis of the wave packages which would provide new insides into the transition process above the porous surface.

6. Numerical Rebuild

6.1. Stability Analysis on Porous Walls

This section summarized the performed numerical stability analyses, including second mode as well as transition predictions. A comparison of the original starting C/C material (see e.g. Wagner et al. Wagner (2014b); Wagner et al. (2013b)) with focus on the experiments, or Wartemann et al. Wartemann et al. (2015), with focus on the numeric), are compared with the new, optimized C/C-SiC, which was developed in the range of this project.

6.1.1. Linear stability approach

For the base flows calculations the DLR TAU code is used. The code is a three-dimensional parallel hybrid multi-grid code and has been validated for hypersonic flows (see e.g. Mack et al. Mack and Hannemann (2002), Schwamborn et al. Schwamborn et al. (2006) or Reimann et al. Reimann and Hannemann (2010)). Axisymmetric grids are applied for the base flow calculations, including grid-point clustering toward the nose, the wall of the cone and the shock.

The stability analysis itself is performed with the stability code NOLOT (NOnLocal Transition analysis, Hein Hein et al. (1994)), which was developed in cooperation between the DLR and the Swedish Defence Research Agency. The NOLOT code can be used for local as well as non-local analyses. In the range of this work the local linear spatial approach is used, which is a subset of the non-local stability equations. Previous investigations of the same geometry with a similar free stream condition, based on a comparison of the experimental / calculated growth rate of the second modes, shows that it is possible to apply LST (linear stability theory) instead of PSE (Parabolized Stability Equations), see e.g. Wartemann Wartemann (2014). For the numerical rebuild of the experiments the stability code NOLOT is applied with an impedance boundary conditions (see e.g. Wartemann et al. Wartemann et al. (2015)).

6.1.2. Applied free stream conditions and material characteristics

In the scope of the numerical study of section 6.1 the HEG conditions listed in table 6-1 are used coverin. a free-stream unit Reynolds number range between $1.6 \times 10^6\,\mathrm{m}^{-1}$ and $6.4 \times 10^6\,\mathrm{m}^{-1}$ at total enthalpies around $3\,\mathrm{MJ/kg}$.

The main material properties, which are used for the numerical analysis, are summarized in table 6-2.

A detailed description of the C/C material properties can be found for example in Wartemann et al. Wartemann et al. (2015). A porous layer thickness of $5mm$ is used, which is (for the present test conditions) above the deep pore limit beyond which an additional absorber thickness does not further increase its effectiveness.
The material properties of the optimized C/C-SiC can be found in Dittert et al. Dittert et al. (2018a). Those are used for the present numerical investigations. That means, the structure factor as well as the specific flow resistivity are expressed as functions of disturbance wave frequency to adapt

6-1 Mean HEG test conditions at Mach 7.5 used for the numerical study.

$\mathrm{Re_m}$ $[\mathrm{m}^{-1}]$	$1.6\,\mathrm{x}\,10^6$	$4.4\,\mathrm{x}\,10^6$	$6.4\,\mathrm{x}\,10^6$
p_0 $[MPa]$	6.7	19	28
T_0 $[K]$	2690	2720	2550
h_0 $[MJ/kg]$	3.2	3.2	3.0
T_∞ $[K]$	260	270	245
ρ_∞ $[g/m^3]$	10	28	42
u_∞ $[m/s]$	2400	2410	2340

the homogenous absorber theory in the best way possible to the experimentally obtained reflection coefficients, as discussed in section 4.4.2. Figure 6-1 provides the absorption coefficient distribution

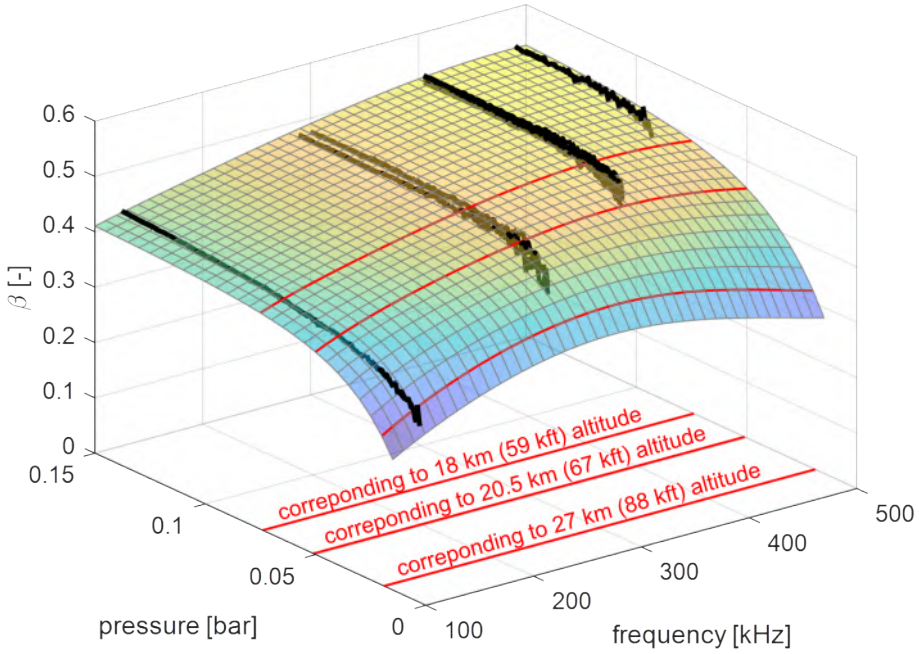

6-1 Absorption coefficient distribution of the C/C-SiC applied in the wind tunnel test campaign in HEG.

as function of frequency and ambient pressure (or equivalent static/surface pressure in flight). The distribution provided in figure 6-1 corresponds to the material properties expressed in table 6-2 and have been used in the subsequent section to predict the transition location above C/C-SiC in the HEG wind tunnel tests.

Towards the end of the project significant improvements in measuring the flow through resistance were made revealing a dependency on the ambient pressure as the rarefied gas regime is reached. This new insight should be used to verify if the present formulation of the absorber properties is still the most accurate formulation possible.

6-2 Material properties used for the homogeneous absorber theory (HAT). The properties are based on the experimentally obtained absorption coefficients between 125 kHz and 490 kHz at static pressures of up to 15000 Pa. Since the assumption of constant structure factor and flow resistivity prevents a good representation of the observed absorption behavior the below properties as function of frequency were introduced.

material	porosity	structure factor	flow resistivity
C/C	14.9%	8	$13.3MPa \cdot s/m^2$
C/C-SiC	15.8%	$4.89E^{-12} \cdot f^2 - 5.28E^{-06} \cdot f + 2.32$	$1.64E^{-11} \cdot f^3 - 6.95E^{-06} \cdot f^2 + 0.91 \cdot f + 290.40E^3$

6.2. Transition predictions versus measurements

For the analyses of the transition prediction the unit Reynolds numbers $Re_{\mathrm{m}} = 4.4 \times 10^6/\mathrm{m}$ and $Re_{\mathrm{m}} = 6.4 \times 10^6/\mathrm{m}$ are chosen (see also table 6-1). For these Reynolds numbers the heat fluxes measurements deliver a clearly visible increase from the laminar to the turbulent level, looking on the smooth reference surface side. Consequently, $Re_{\mathrm{m}} = 4.4 \times 10^6/\mathrm{m}$ and $Re_{\mathrm{m}} = 6.4 \times 10^6/\mathrm{m}$ are predestined for the numerical transition prediction.

As before in section 5.1.2, for the LST prediction of the numerical, relative transition delay, the semi-empirical approach of the e^N-method is applied. The measured transition x-coordinate of the C/C surface side are from a previous wind tunnel test campaign of the HEG (see Wagner et al. Wagner (2014b); Wartemann et al. (2015)). The measured transition x-coordinate of the C/C-SiC surface side are depicted in figure 5-12. The measured $x_{\mathrm{trans,smooth}}$ of fig. 5-12 delivers the corresponding $N_{\mathrm{trans,smooth}}$. This $N_{\mathrm{trans,smooth}}$ is used for the prediction of the transition shift. Figure 6-2.b summarized the transition shift of the C/C material (red color) and the improved C/C-SiC material (green color). The second mode damping of the C/C-SiC material is significant higher, compared to the C/C material. Consequently, the resulting predicted transition shift is also higher. Figure 6-3 depicts the results for $Re_{\mathrm{m}} = 6.4 \times 10^6/\mathrm{m}$. As expected, the predicted shift for the

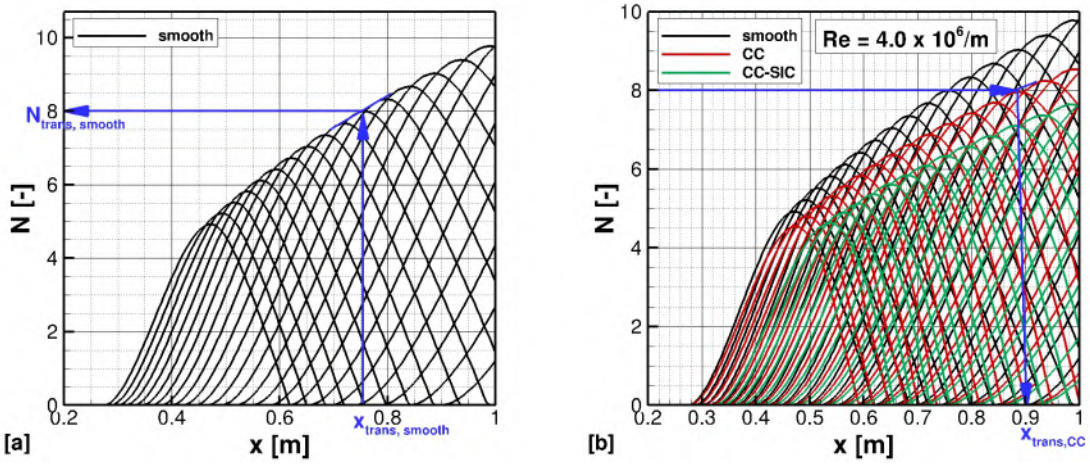

6-2 Transition prediction, using e^N-method, $\mathrm{Re_m} = 4.4 \cdot 10^6 m^{-1}$.

new, optimized C/C-SiC material is also for this test case higher than for C/C. Table 6-3 summarized the comparison of the predicted and measured transition delay. For the C/C-SiC material side at

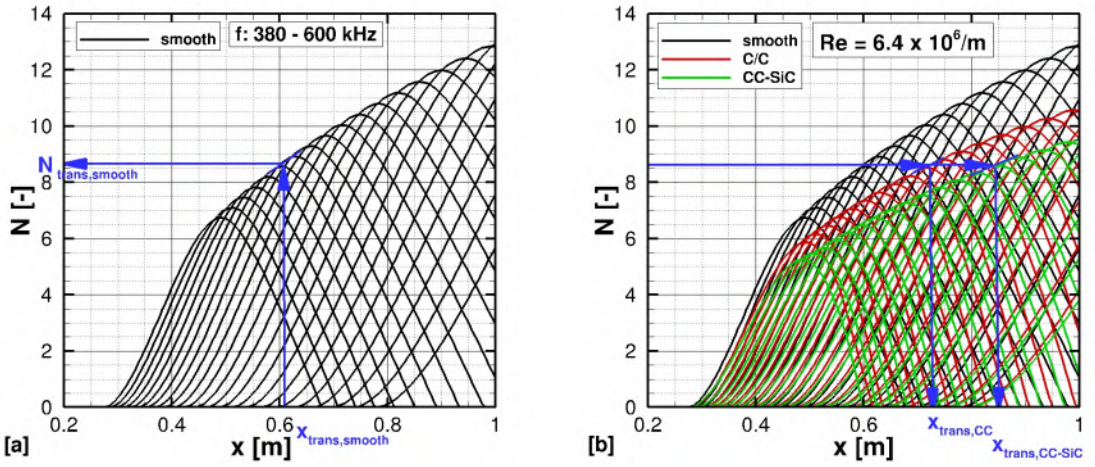

6-3 Transition prediction, using e^N-method, $\mathrm{Re_m} = 6.4 \cdot 10^6 m^{-1}$.

the lower unit Reynolds number $\mathrm{Re_m} = 4.4 \cdot 10^6 m^{-1}$ the heat flux measurements shows a laminar flow, whereas NOLOT predicts only a transition shift in direction of the cone end. Also for the test case with higher unit Reynolds number $\mathrm{Re_m} = 6.4 \cdot 10^6 m^{-1}$ NOLOT predicts a lower second mode damping. These differences are investigated in more detail by looking at the second mode comparison (see next section 6.2.1).

6-3 Comparison: Transition delay - numerics/experiments.

Re_m [10^6/ m]	$(Re_{\mathrm{trans,porous}} - Re_{\mathrm{trans,smooth}})/Re_{\mathrm{trans,smooth}}$			
	C/C: Exp.	C/C : LST	C/C – SiC : Exp	C/C – SiC : LST
4.4	0.15 Wagner (2014b)	0.18 Wartemann et al. (2015)	laminar	0.25
6.4	0.20 Wagner (2014b)	0.20 Wartemann et al. (2015)	0.35	0.23

6.2.1. Second mode comparison: LST versus measurements

Two requirements are necessary to compare the numerically obtained second mode amplitude against experimental data: First, the signal to noise ratio of the second mode instability at the pressure transducer position has to be high enough. Second, the flow at the transducer position has to be laminar. Otherwise, a decomposition of the second mode due to the transition process is possible which does not allow to compare the measurements with the linear, laminar predictions of NOLOT. Thus, a test case with a low unit Reynolds number was chosen: $1.6 \cdot 10^6 m^{-1}$. For this free stream condition at all sensor positions the second mode is clearly measurable and a laminar boundary layer was observed on the smooth surface side, except at the last transducer location.

Figure 6-4 shows the measured amplitude spectral density (ASD) on the right ordinate. It was derived by conducting a discrete Fourier transformation of the measured pressure fluctuations recorded in the test time, as a function of the measured frequency marked as symbols. The measurements on the smooth surface are marked with black color, the measurements on the porous surface with red. The same colors are used for the LST calculations ($e^N = f(f)$). The $\mathrm{LST_{CC}}$ calcu-

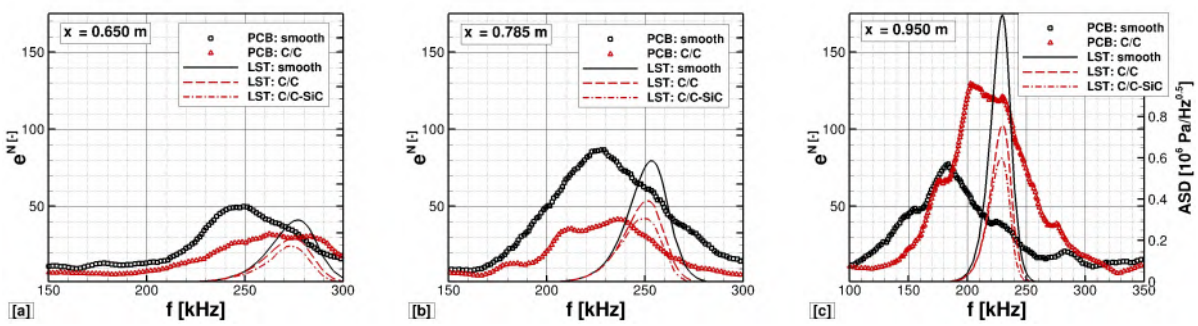

6-4 Comparison: measured/calculated second modes.

lations are illustrated as dashed lines and the LST calculations for the C/C-SiC material ($\mathrm{LST}_{\mathrm{CC-SiC}}$) are marked with dashed dot lines. As expected, the calculated/measured second mode is amplified in streamwise direction. Due to the increase of the boundary-layer thickness the frequencies of the second modes were shifted to lower values, which can be explained with the following relation between the boundary-layer thickness δ and the wavelength λ Mack (1984): $\lambda \approx 2\,\delta$. Thermocouple readings at the most rear position on the cone revealed, that the last sensor position on the smooth surface was already in the transitional regime. Hence, the mode was decomposed due to the transition process which does not allow to compare the measured second mode at the last sensor location with the laminar LST predictions. In conclusion, an analysis of the instability damping at that position is not possible either. Further the thermocouples showed, that on the porous surface the boundary-layer flow is completely laminar, which is also in agreement with the LST predictions.

The measured ASD data cannot be compared directly with the numerically calculated e^N-values. However, it is possible to compare the damping of the second mode and its frequency range. The comparison of the calculated/measured frequency range shows a difference of about $10\,\%$. Theses differences result from the approach for the base flow calculations. Recent analyses have shown, that the base flow simulations should include the nozzle, test chamber, and cone model itself Wartemann et al. (2019), which reduced the shift of the frequency between measurements and calculations of around 5% (depending on the free stream conditions / test case). Analysing the damping of the second modes due to the C/C material, demonstrated a comparable reduction of the measured / calculated second mode (see figure 6-4.a and b). The measurements for the new, optimized C/C-SiC material are not included in the pictures, because the measured second modes are completely damped. Like in the previous section 6.2, the numerical predictions for C/C-SiC delivers a lower damping of the second modes as visible in the measurements. One possible reason could be the applied material data (see table 6-2). The recent findings of the last weeks show a change of the functions for the structure factor and the flow resistivity of table 6-2. Another explanation is the higher surface porosity in the experiments illustrated in figure 4-13, which can not be reproduced with LST. The LST calculations are with a lower, constant porosity. Only a study of different constant porosity is possible and also planned. A complete reproduction of the varied porosity over the depth is only with DNS possible and recommend. Nevertheless, the numerical investigations demonstrate, as in the experiments, an improvement of the material (comparing C/C with C/C-SiC) in respect to the second mode damping and the resulting transition delay.

7. Conclusion

Overall, it can be concluded that temperature stable porous C/C-SiC based material can be developed and tailored such that an application as Ultrasonically Absorptive Thermal Protection System (UAT) is possible.

Materials
A feasibility study on different material manufacturing processes revealed advantages and disadvantages of each process. In conclusion, a process was developed providing material with adequate absorber and TPS properties and acceptable manufacturing costs. Large improvement is identified in the field of cost effective manufacturing combined with an desired increased flexibility with respect to curved surfaces, see section 9 on proposed future work.
Significant improvement were realized in the course of the project with respect to the material characterization. All methods required to determine the absorber efficiency; i.e. flow through resistance, absorption measurements, porosity; reached a level of maturity allowing to predict the absorber performance for different frequencies and pressures in conjunction with the homogenous absorber theory.

Experimental Testing
The test campaign in HEG experimentally confirmed the expected transition delay capabilities of the UAT material. Strong second mode damping and strong transition delay was observed. The UAT material was found to perform significantly better compared to the original C/C. Furthermore, valuable experience in the field of instrumenting and integration of UAT materials was gathered.

Numerical Rebuild
The LST based prediction of the boundary layer transition location unpredicted the UAT performance using an impedance boundary condition based on the homogeneous absorber theory. A possible reason could be a too conservative absorber property description not taking into account the latest findings in the material characterization. In conclusion, the numerical method is in place while the absorber properties need to be updated to match the experimental results.

8. Dissemination

Two particular aspects of the present study were presented on the *2018 AIAA Aviation and Aeronautics Forum and Exposition* in Atlanta in June 2018. The two corresponding papers are:

- Process Optimization of Ceramic Matrix Composites for Ultrasonically Absorptive TPS Material presented by Dittert et al. (2018b)
- Experimental and numerical acoustic characterization of ultrasonically absorptive porous materials presented by Wagner et al. (2018).

The following two publications are foreseen at the AIAA Aviation Conference in 2020:

- Concluding the Development of CC-SiC as Ultrasonically Absorptive Thermal Protection Material for Hypersonic Transition Suppression - **Part 1** by Wagner, Wartemann and Dittert
- Concluding the Development of CC-SiC as Ultrasonically Absorptive Thermal Protection Material for Hypersonic Transition Suppression - **Part 2** by Wartemann, Wagner and Dittert.

9. Suggested Future Work

9.1. UAT with Increased Shaping Flexibility

An Ultrasonically Absorptive Thermal Protection material (UAT) was developed in DLR. After it was successfully demonstrated that the high-temperature resistant C/C-SiC can be designed, manufactured, characterized and applied to delay hypersonic boundary layer transition it is time to identify the next steps beyond the demonstration of feasibility.

The following aspects were identified:

1. optimization with respect to cost-effectiveness and shaping flexibility for the UAT to expand its field of application
2. the impact of the type of textile weave and their orientation on the porosity and permeability of the final UAT should be further investigated
3. stitching techniques like tufting, which introduces a non-stable fiber material in the z-direction of the fabric to generate channel cavities should be explored to allow maximum shape flexibility
4. it should be investigated if a "classic" TPS structure, consisting of a rigid ceramic surface panel of 2-3mm thickness and a fibrous ceramic layer underneath, can be implemented with the ultrasonic absorptive properties. Consequently, a UAT TPS would be suitable for flight applications as it is able to deflect mechanical loads reliably.
5. manufacturing technologies should be evaluated in terms of their suitability for large hypersonic vehicles, including their acoustic properties, as well as for their reliability and economic viability.

9.2. Transpiration Cooling with UAT

Another research opportunity is the use of UAT TPS in combination with the concept of transpiration cooling, where a coolant passes through the porous skin of an hypersonic vehicle, forming a protective insulation layer between the hot air in the boundary layer and the outer surface of the vehicle Rubesin (1954). At DLR, the technologies to control the outflow through porous material are well known Dittert et al. (2018b), Böhrk (2015). However, introducing the coolant into the high-speed boundary layer could cause unwanted instabilities, eventually leading to laminar-turbulent transition. The use of UAT TPS could compensate for these disturbances, leading to an improved efficiency of hypersonic vehicles.

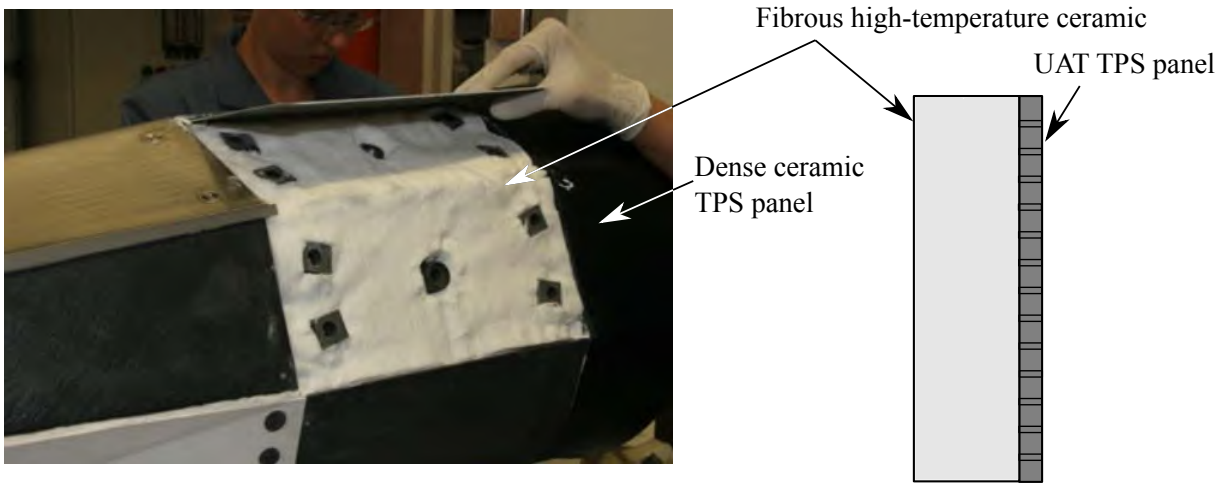

9-1 Left: Dense C/C-SiC standard TPS as mounted on SHEFEX I Weihs (2013b).) Right: Proposed design of an UAT TPS.

Bibliography

A. V. Fedorov, Norman D. Malmuth, A. Rasheed, and H. G. Hornung. Stabilization of hypersonic boundary layers by porous coatings. AIAA, 39(4):605–610, April 2001.

A. Rasheed, H. G. Hornung, A. V. Fedorov, and N. D. Malmuth. Experiments on passive hypervelocity boundary-layer control using an ultrasonically absorptive surface. AIAA, 40(3):481–489, March 2002.

A. V. Fedorov, V. Kozlov, A. Shiplyuk, A. Maslov, and N. Malmuth. Stability of hypersonic boundary layer on porous wall with regular microstructure. AIAA Journal, 44(8):1866–1871, August 2006.

A. Wagner, M. Kuhn, J. Martinez Schramm, and K. Hannemann. Experiments on passive hypersonic boundary layer control using ultrasonically absorptive carbon-carbon material with random microstructure. Experiments in Fluids, 54(10), 2013a. ISSN 0723-4864. doi: 10.1007/s00348-013-1606-3.

A. Wagner, K. Hannemann, and M. Kuhn. Ultrasonic absorption characteristics of porous carbon-carbon ceramics with random microstructure for passive hypersonic boundary layer transition control. Experiments in Fluids, 55(6):1750, 2014. doi: 10.1007/s00348-014-1750-4.

V. Wartemann, A. Wagner, M. Kuhn, T. Eggers, and K. Hannemann. Passive hypersonic boundary layer transition control using an ultrasonically absorptive coating with random microstructure: Computational analysis based on the ultrasonic absorption properties of carbon-carbon. In IUTAM ABCM Symposium on Laminar Turbulent Transition, Rio de Janeiro, Brasil, September 2014.

H. Weihs, H. Hald, T. Reimer, and I. Fischer. Development of a CMC nose cap for X-38. In 52nd International Astronautical Congress, Toulouse, France, October 2001.

T. Reimer. The KERAMIK thermal protection system experiment on the FOTON-M2 mission. In 5th European Workshop on Thermal Protection Systems and Hot Structures, Nordwijk, 2006. ESA.

H. Weihs. Sounding rockets for entry research: SHEFEX flight test program. In L. Ouwehand, editor, 21st ESA Symposium on European Rocket and Balloon Programmes and related Research, volume SP-721 of ESA Proceedings, pages 143–152. ESA Communications, October 2013a.

D. E. Glass, D. G. Capriotti, T. Reimer, M. Kütemeyer, and M. Smart. Testing of DLR C/C-SiC and C/C for HIFiRE 8 scramjet combustor. In Proc-19th AIAA" International Space Planes and Hypersonic Systems and Technologies Conference", Atlanta, Georgia, 2014.

W. Krenkel. Ceramic Matrix Composites: Fiber Reinforced Ceramics and Their Applications. Wiley, 2008. ISBN 9783527313617.

C. Zuber, T. Reimer, K. Stubicar, B. Heidenreich, and H. Hald. Manufacturing of the cmc nose cap for the expert spacecraft. In ICACC 2010, Januar 2010. URL `http://elib.dlr.de/67307/`.

Hendrik Weihs. Sounding rockets for entry research: SHEFEX flight test program. In 21st ESA Symposium on Rocket and Balloon Programmes, 2013b.

A. Wagner. Passive Hypersonic Boundary Layer Transition Control Using Ultrasonically Absorptive Carbon-Carbon Ceramic with Random Microstructure. PhD thesis, Ph.D. thesis, Katholieke Universiteit Leuven, 2014a.

C. Dittert and M. Kütemeyer. Octra - optimized ceramic for hypersonic applications with transpiration cooling. In Mrityunjay Singh, Tatsuki Ohji, Shaoming Dong, Dietmar Koch, Kiyoshi Shimamura, Bernd Clauss, and Bernhard Heidenreich, editors, Advances in High Temperature Ceramic Matrix Composites and Materials for Sustainable Development, volume 263 of Ceramic Transaction Series. John Wiley & Sons, Juni 2017. URL http://elib.dlr.de/114540/.

A. Wagner, V. Wartemann, K. Hannemann, Markus Kuhn, and Christian Dittert. The potential of ultrasonically absorptive tps materials for hypersonic vehicles. In 20th AIAA International Space Planes and Hypersonic Systems and Technologies Conference, number AIAA 2015-3576, 2015.

Ferdinand Dömling. Herstellung hochporöser c/c-sic keramiken und deren charakterisierung hinsichtlich der akustischen eigenschaften. Master's thesis, TU Illmenau, 2018.

M. Möser. Technische Akustik. VDI-Buch. Springer, 2009. ISBN 9783540898177. URL https://books.google.de/books?id=1hWk1ZrmSWwC.

E. W. Washburn. The dynamics of capillary flow. Physical Review, 17:273–283, March 1921. doi: 10.1103/PhysRev.17.273. URL http://link.aps.org/doi/10.1103/PhysRev.17.273.

A. V. Fedorov, V. F. Kozlov, and R. C. Addison. Reflection of acoustic disturbances from a porous coating of regular microstructure. In 5th AIAA Theoretical Fluid Mechanics Conference, 2008. AIAA 2008-3902.

G. A. Brès, Tim Colonius, and A. V. Fedorov. Acoustic properties of porous coatings for hypersonic boundary-layer control. AIAA Journal, 48(2):267–274, February 2010. doi: 10.2514/1.40811.

T. Kreis. Holographic interferometry. Akademie Verlag, Berlin, 1996.

C. Roddier and F. Roddier. Interferogram analysis using fourier transform techniques. Applied optics, 26:1668–73, May 1987.

Suezou Nakadate and Hiroyoshi Saito. Fringe scanning speckle-pattern interferometry. Appl. Opt., 24(14):2172–2180, Jul 1985. doi: 10.1364/AO.24.002172. URL http://ao.osa.org/abstract.cfm?URI=ao-24-14-2172.

C. M. Vest. Holographic interferometry. Wiley, New York, 1979.

M. Kujawinska. Spatial phase measurement methods. Interferogram Analysis, 1993. URL https://ci.nii.ac.jp/naid/10016235849/en/.

A. Wagner. Passive Hypersonic Boundary Layer Transition Control Using Ultrasonically Absorptive Carbon-Carbon Ceramic with Random Microstructure. PhD thesis, Katholieke Universiteit Leuven, 2014b. URL https://lirias.kuleuven.be/handle/123456789/463042.

V. Wartemann, A. Wagner, M. Kuhn, T. Eggers, and K. Hannemann. Passive hypersonic boundary layer transition control using an ultrasonically absorptive coating with random microstructure: Computational analysis based on the ultrasonic absorption properties of carbon-carbon. volume Vol. 14. Elsevier, 2015. doi: 10.1016/j.piutam.2015.03.068.

G. Eitelberg, T. J. McIntyre, W. H. Beck, and J. Lacey. The High Enthalpy Shock Tunnel in Göttigen. In 17th AIAA Aerospace Ground Testing Conference, 1992. AIAA 92-3942.

G. Eitelberg. First results of calibration and use of the HEG. In 18th AIAA Aerospace Ground Testing Conference, 1994. AIAA 94-2525.

Deutsches Zentrum für Luft - und Raumfahrt (DLR). The High Enthalpy Shock Tunnel Göttingen of the German Aerospace Center (DLR). Journal of large-scale research facilities, 4, A133, 2018. doi: http://dx.doi.org/10.17815/jlsrf-4-168.

A. Wagner, K. Hannemann, V. Wartemann, and T. Giese. Hypersonic boundary-layer stabilization by means of ultrasonically absorptive carbon-carbon material - part 1: Experimental results. In 51st AIAA Aerospace Sciences Meeting, Texas, January 2013b. doi: 10.2514/6.2013-270. URL http://dx.doi.org/10.2514/6.2013-270. AIAA 2013-0270.

A. Mack and V. Hannemann. Validation of the unstructured DLR-TAU-Code for hypersonic flows. In 32nd AIAA Fluid Dynamics Conference and Exhibit, St. Louis, Missouri, 2002. AIAA 2002-3111.

D. Schwamborn, T. Gerhold, and R. Heinrich. The dlr tau-code: Recent applications in research and industry. In European Conference on Computational Fluid Dynamics ECCOMAS CFD, 2006.

B. Reimann and V. Hannemann. Numerical investigation of double-cone and cylinder experiments in high enthalpy flows using the dlr tau code. In 48th AIAA Aerospace Sciences Meeting Including the New Horizons Forum and Aerospace Exposition, 2010. doi: 10.2514/6.2010-1282.

S. Hein, F. P. Bertolotti, M. Simen, A. Hanifi, and D. Henningson. Linear nonlocal instability analysis - the linear NOLOT code. Technical Report IB-223-94 A56, DLR, 1994.

V. Wartemann. Mack-Moden-Dämpfung mittels mikroporöser Oberflächen im Hyperschall. PhD thesis, Technische Universität Braunschweig, 2014.

C. Dittert, M. Kütemeyer, M. Kuhn, and A. Wagner. Process optimization of ceramic matrix composites for ultrasonically absorptive tps material. In AIAA Aviation, Joint Thermophysics and Heat Transfer Conference, 2018a. doi: 10.2514/6.2018-2947.

L. M. Mack. Boundary layer linear stability theory. AGARD - Special Course on Stability and Transition of Laminar Flow, 1984.

V. Wartemann, A. Wagner, R. Wagnild, F. Pinna, F. Miró Miró, H. Tanno, and H. Johnson. High enthalpy effects on hypersonic boundary layer transition. Journal of Spacecraft and Rockets, 56 (2), 2019. doi: 10.2514/1.A34281.

C. Dittert, M. Kütemeyer, M. Kuhn, and A. Wagner. Process optimization of ceramic matrix composites for ultrasonically absorptive tps material. In 2018 AIAA Aviation and Aeronautics Forum and Exposition, 2018b.

A. Wagner, E. Schülein, R. Petervari, K. Hannemann, S. R. C. Ali, A. Cerminara, and N. D. Sandham. Combined free-stream disturbance measurements and receptivity studies in hypersonic wind tunnels by means of a slender wedge probe and direct numerical simulation. Journal of Fluid Mechanics, 842:495–531, 2018. doi: 10.1017/jfm.2018.132.

Morris W. Rubesin. An analytical estimation of the effect of transpiration cooling on the heat-transfer and skin-friction characteristics of a compressible, turbulent boundary layer. In National Advisory Commitee for Aeronautics, volume 3341 of Technical Note. Ames Aeronautical Laboratory, December 1954.

Hannah Böhrk. Transpiration-cooled hypersonic flight experiment: Setup, flight measurement, and reconstruction. Journal of Spacecraft and Rockets, 2015. doi: 10.2514/1.A33144. URL `http://dx.doi.org/10.2514/1.A33144`.

Register of illustrations

List of tables